Received: 13 March 2022 | Revised: 15 April 2022 | Accepted: 26 April 2022

DOI: 10.1002/cne.25339

RESEARCH ARTICLE

JCN RESEARCH IN SYSTEMS NEUROSCIENCE THE JOURNAL OF COMPARATIVE NEUROLOGY WILEY

A three-dimensional atlas of the honeybee central complex, associated neuropils and peptidergic layers of the central body

Andreas Kaiser[1] | Ronja Hensgen[1] | Katja Tschirner[2] | Evelyn Beetz[2] | Hauke Wüstenberg[1] | Marcel Pfaff[2] | Theo Mota[3] | Keram Pfeiffer[1,2]

[1]Department of Biology/Animal Physiology, Philipps-University Marburg, Marburg, Germany

[2]Behavioural Physiology and Sociobiology (Zoology II), Biocenter, University of Würzburg, Würzburg, Germany

[3]Department of Physiology and Biophysics, Federal University of Minas Gerais, Belo Horizonte, Brazil

Correspondence
Keram Pfeiffer, Behavioural Physiology and Sociobiology (Zoology II), Biocenter, University of Würzburg, Würzburg 97074, Germany.
Email: keram.pfeiffer@uni-wuerzburg.de

Funding information
Deutsche Forschungsgemeinschaft (DFG), Grant/Award Numbers: PF 714/4-1, PF714/5-1, INST160/447-1FUGG, INST93/829-1FUGG; FAPEMIG - Minas Gerais Research Funding Foundation, Grant/Award Number: APQ-02711-21

Abstract

The central complex (CX) in the brain of insects is a highly conserved group of midline-spanning neuropils consisting of the upper and lower division of the central body, the protocerebral bridge, and the paired noduli. These neuropils are the substrate for a number of behaviors, most prominently goal-oriented locomotion. Honeybees have been a model organism for sky-compass orientation for more than 70 years, but there is still very limited knowledge about the structure and function of their CX. To advance and facilitate research on this brain area, we created a high-resolution three-dimensional atlas of the honeybee's CX and associated neuropils, including the posterior optic tubercles, the bulbs, and the anterior optic tubercles. To this end, we developed a modified version of the iterative shape averaging technique, which allowed us to achieve high volumetric accuracy of the neuropil models. For a finer definition of spatial locations within the central body, we defined layers based on immunostaining against the neuropeptides locustatachykinin, FMRFamide, gastrin/cholecystokinin, and allatostatin and included them into the atlas by elastic registration. Our honeybee CX atlas provides a platform for future neuroanatomical work.

KEYWORDS
average shape brain atlas, central complex, honeybee, navigation, neuropeptides, optic tubercle, spatial orientation

1 | INTRODUCTION

The central complex (CX) is a group of midline-spanning neuropils in the center of the insect brain. It consists of the central body with its upper division (CBU, fan-shaped body in some insect species), its lower division (CBL, ellipsoid body in some insect species), the protocerebral bridge (PB), and the paired noduli (NO). The CX houses the internal compass of insects and is involved in goal-directed behaviors, sleep regulation, and decision making (Pfeiffer & Homberg, 2014). In many insects including tropical sweat bees, electrophysiological evidence has suggested that the CX is involved in sky-compass orientation (locust: Heinze & Homberg, 2007, cricket: Sakura et al., 2008, monarch butterfly: Heinze & Reppert, 2011, dung beetle: el Jundi et al., 2015, sweat bee: Stone et al., 2017, *fruit fly*: Hardcastle et al., 2021). Further work in *Drosophila* shows that the internal compass in the CX can also be driven by other visual stimuli, proprioceptive feedback, and wind information (Okubo et al., 2020; Seelig & Jayaraman, 2015).

Visual information enters the CX via two parallel pathways from the eye through the anterior optic tubercle. Neuronal signals related to celestial cues are processed and relayed by the sky-compass pathway, also called the anterior visual pathway (Hardcastle et al., 2021; Held et al., 2016; Zeller et al., 2015). Polarized light information of the sky is picked up by the dorsal rim area of the eye and is processed in the optic lobes and relayed to the lower unit complex of the anterior optic tubercles (AOTU-LUC, locust: Homberg et al., 2003; Pfeiffer et al., 2005, honeybee: Mota et al., 2011; Zeller et al., 2015, bumblebee: Pfeiffer & Kinoshita, 2012). In locusts, it has been shown that this neuropil also processes unpolarized light information about solar azimuth and the chromatic contrast of the sky (Kinoshita et al., 2007; Pfeiffer & Homberg, 2007). From the AOTU-LUC, sky-compass information is forwarded to the lateral and medial bulbs of the lateral complex, which in turn provide input to the CBL (Held et al., 2016). Unpolarized light information is passed through the upper unit of the anterior optic tubercle to the lateral accessory lobe and likely enters the CBU from there (Homberg et al., 2003).

Honeybees are well known for their exquisite orientation capabilities as central place foragers and have long been a behavioral model organism for learning and sky-compass orientation (von Frisch, 1965). Yet, little is known about the neurobiology of the honeybee's CX. Some details are described in older neuroanatomical work (Jonescu, 1909; Kenyon, 1896; Mobbs, 1985) and two studies report responses of honeybee CX neurons to visual, mechanical, and olfactory stimuli (Homberg, 1985; Milde, 1988). A more recent study from our group provides an anatomical description of neuronal cell types in the CX of honeybees (Hensgen et al., 2020). Many of these neurons have also been found in the highly similar CX of bumblebees (Sayre et al., 2021). Here, we extend this base by providing a three-dimensional atlas of the honeybee's CX and associated neuropils, which includes distinct layers of the central body derived from neuropeptidergic immunostaining. The insect CX is heavily innervated by peptidergic neurons (Galizia & Kreissl, 2012; Kahsai & Winther, 2011; Kreissl et al., 2010; Nässel & Homberg, 2006; Schürmann & Erber, 1990; Strausfeld et al., 2000). While there is only little known about the functions of neuropeptides in the insect CX (Kahsai et al., 2010; Sareen et al., 2021), immunostainings against peptides have been used for a long time as a neuroanatomical tool that help to understand the neuronal organization of the brain.

Three-dimensional brain atlases are important tools in neuroanatomical research and are becoming available for increasing numbers of insect species (for a review see: el Jundi & Heinze, 2020, jewel wasp: Groothuis et al., 2019, bumblebee: Rother et al., 2021). They allow coregistration of neurons or neuronal populations into a common frame of reference and to make predictions about potential overlap of branching areas (el Jundi et al., 2010). One of the first insect brain atlases was the one of the honeybee (Brandt et al., 2005). This atlas, however, had its focus rather on the mushroom bodies than the CX, which is only represented as a single neuropil that includes CBU, CBL, and the NO, but not the PB. Furthermore, due to limited hardware power in 2005, the resolution of the honeybee standard brain atlas had to be restricted to $3.8 \times 3.8 \times 8\ \mu m^3$. To get the most out of a brain atlas, it is desirable to have a high spatial resolution and a clear compartmentalization. Also, the compartments need to be easy to reproduce experimentally by other researchers. We therefore created a standard atlas with a voxel size of $0.76 \times 0.76 \times 1.5\ \mu m^3$ and layers of the central body that are based on peptidergic immunostaining. These stainings are easy to reproduce and can be combined with general neuropil staining techniques as well as with tracing methods. This will facilitate future neuroanatomical work on the honeybee's CX.

2 | MATERIALS AND METHODS

2.1 | Animals

Honeybee colonies were maintained at the University of Marburg and at the Ecological Station of the Federal University of Minas Gerais (Belo Horizonte, Brazil). Honeybees were kept outdoors during the whole year in Belo Horizonte and between April and October in Marburg. Between October and April, hives in Marburg were moved to a greenhouse, where they were kept under natural light conditions at a temperature of 20–25°C and relative humidity between 60 and 80%. Bees in the greenhouse could freely forage for ground pollen and honey water (20–30% v/v) within a volume of 2 m × 2 m × 2 m. Foraging worker bees were caught as they were leaving the hive, or at the feeding site in the greenhouse.

2.2 | Osmium staining

Osmium staining was used to assess the general anatomy of the honeybee's CX. This contrasting technique, which has been previously used in honeybees (Mota et al., 2011), allows to visualize neuropils (appearing dark), while at the same time, tracts are not, or only weakly stained and appear in lighter shades of gray, thus allowing to assess both the structure of neuropils and tracts. Foragers were collected from a feeder containing 30% (v/v) sugar solution, 50 meters from the hives. Each bee was cold anesthetized in a small glass vial for two min and then decapitated. The head was fixed in a small bowl containing hard beeswax and opened frontally with a fine scalpel blade. The brain was carefully dissected out under phosphate-buffered saline (PBS) (1×, containing in g/L: Na_2HPO_4, 1.78; KH_2PO_4, 0.24; NaCl, 8.0; KCl, 0.2, pH 6.8) and fixed for 12 h at 4°C in phosphate-buffered 4% formaldehyde solution (pH 6.8; Sigma–Aldrich/Merck, Brazil; catalog No.: 100496). Brains were rinsed four times in PBS 1 (10 min under agitation) and then stained in 1% aqueous osmium tetroxide solution for 2 h at 4°C, and one additional hour at room temperature. After this period, brains were rinsed three times in water (1 h under agitation), dehydrated in ascending concentrations of ethanol (35, 50, 70, 90, 95, and 100%; 10 min each), embedded in glycol methacrylate (Technovit® H7100; Electron Microscopy Sciences, Hatfield, PA, USA) and polymerized at 40°C. Brains were sectioned on a sliding microtome (Biocut 2030; Leica ReichertJung, Germany) at 10 µm thickness, mounted on glass slides with Entellan (Merck, Darmstadt, Germany) and coverslipped.

TABLE 1 Primary antibodies used in this study

Antibody	Dilution	Raised in	Immunogen	Reference	Source	RRID
Synapsin	1:50	Mouse	SYN1	Klagges et al. (1996)	Dr. E. Buchner/Dr. C. Wegener (Würzburg, Germany)	AB_2315425
Dip-Ast A	1:10,000	Rabbit	APSGAQRLYGFGLamide	Vitzthum et al. (1996)	Dr. H. Agricola (Jena, Germany)	AB_2313971
FMRFamide # 671N	1:4000	Rabbit	FMRFamide	Marder et al. (1987)	Dr. E. Marder (Brandeis Univ., USA)	AB_2314417
LomTK II	1:10,000	Rabbit	APLSGFYGVRamide	Veenstra et al. (1995)	Dr. H. Agricola (Jena, Germany)	AB_2341129
Gastrin/cholecystokinin #1199	1:500	Rabbit	CCK 1–26	Homberg et al. (1991)	J. Polak (London, UK)	NA

2.3 | Antibody characterization

For immunolabeling, we used polyclonal antibodies against FMRFamide, allatostatin-A (AST), locustatachykinin II (LomTK II), gastrin/cholecystokinin, and a monoclonal antibody against the synaptic vesicle protein synapsin (Table 1). All antisera were originally donated to Dr. Uwe Homberg, who kindly shared them with us.

The FMRFamide antiserum (No. 671N; RRID: AB_2314417) was donated by Dr. Eve Marder (Brandeis University, USA). It was raised in rabbit against synthetic FMRFamide conjugated to thyroglobulin (Marder et al., 1987). Specificity tests by radioimmunoassay showed cross-reactivity of the antiserum with various N-terminally extended RFamides (Marder et al., 1987).

The AST antiserum (RRID: AB_2313971) was a donation from Dr. Hans Agricola (University of Jena, Germany). It was raised in rabbit against *Diploptera punctata* allatostatin I (APSGAQRLYGFGLamide) coupled to bovine thyroglobuline using glutaraldehyde. Competitive enzyme-linked immunosorbent assay (ELISA) showed that the antiserum cross-reacts with other members of the A-type allatostatin family that carry a C-terminal Y/FXFGLamide (Vitzthum et al., 1996). Preadsorption with 10 μmol L^{-1} Dip-allatostatin I abolished all immunostaining in brain sections of *Schistocerca gregaria* (Vitzthum et al., 1996). Preadsorption with 1 μmol L^{-1} Dip-allatostatin I abolished all immunostaining in whole mount brain preparations of *Aedes aegypti* (Siju et al., 2014).

The LomTK II antiserum (K1-50820091; RRID: AB_2341129) was donated by Dr. Hans Agricola. It was raised in rabbit against the full LomTK II peptide (APLSGFYGVR-NH_2) (Veenstra et al., 1995). ELISA with synthetic LomTK I and II and callitachykinins I and II as antigens demonstrated specificity (Nässel et al., 1995). In *S. gregaria*, immunostaining was completely abolished by preadsorption of the antiserum with 10 μmol L^{-1} synthetic LomTK II (Vitzthum & Homberg, 1998).

The antiserum against gastrin/cholecystokinin (CCK; # 1199) was donated by Dr. Julia Polak (Imperial College of London). It was raised in rabbit against CCK 1–26 (Davis et al., 1996). Its specificity was previously demonstrated by liquid-phase preadsorption experiments in various insects. Immunostaining was abolished by 200 nmol L^{-1} CCK8 in *Manduca sexta* (Homberg et al., 1991), 10 μmol L^{-1} CCK8 in *S. gregaria* (Würden & Homberg, 1995), 40 μmol L^{-1} CCK 26–33 in *Rhyparobia maderae* (Petri et al., 1995), and 1 μmol L^{-1} gastrin/CCK in *Apis mellifera* (Strausfeld et al., 2000).

The monoclonal antibody against the synaptic vesicle protein synapsin (SYNORF1, RRID: AB_2315425) was donated by Drs. Erich Buchner/Christian Wegener (University of Würzburg, Germany). It was raised in mouse against fusion proteins of glutathione-S-transferase and *Drosophila* SYN1 protein (Klagges et al., 1996). The specificity of the antibody has been characterized by Klagges et al. (1996). This antibody has been previously used as a neuropil marker in a variety of insect species, including honeybees (Brandt et al., 2005; Held et al., 2016; Zeller et al., 2015).

2.4 | Gelatin sections

Before dissection, animals were chilled on ice for 15 min and waxed to a custom-made perspex holder. Immediately after opening the head capsule frontally, a drop of fixative was added. This was either 4% paraformaldehyde (Merck, Darmstadt, Germany) for gastrin/cholecystokinin or 4% formaldehyde made from a 37% formaldehyde solution that contained 10% methanol for stabilization (Rotipuran 37%; p.a. ACS, Roth, Karlsruhe, Germany) for all other peptide antisera. Fixative solutions were buffered by 0.1 M PBS (containing in g/L: $Na_2HPO_4 \cdot 2\ H_20$, 14.02; $NaH_2PO_4 \cdot H_20$: 2.62; pH 7.4). Glands, trachea, and air sacs were removed to expose the brain, which was then dissected from the head capsule. After removing the outer neural sheath, the brain was fixated overnight at 4°C or for at least 1 h at room temperature. After four 15 min rinses in sodium phosphate buffer (containing: 100 ml PBS, 900 ml H_20, and 8.8 g NaCl; pH 7.4), brains were embedded in albumin gelatin (12% ovalbumin, 4.8% gelatin in demineralized water) and fixated overnight at 4°C with 8% formaldehyde in 0.1 M PBS. The next day, brains were sectioned in the frontal or sagittal plane at 40 μm using a vibrating blade microtome (VT1200 S; Leica Microsystems, Wetzlar, Germany). All following steps including incubation with antisera were carried out at room

temperature under agitation. Slices were rinsed for 4 × 15 min in saline substituted Tris-buffer (SST, pH 7.4, containing in g/L: NaCl, 17.53; Tris/HCl, 13.22; Tris base, 1.94) with 0.1% Triton-X 100 (TrX). To block unspecific binding sites, sections were preincubated in 5% normal goat serum (NGS; Jackson ImmunoResearch, West Grove, PA, USA; catalog No. 005-000-121, RRID: AB_2336990) in SST with 0.5% TrX. After 1 h, the blocking solution was removed, and the primary antibody solution was added. It consisted of the primary antibody (see Table 1 for dilutions of primary antibodies), 1% NGS and 0.5% TrX in SST. After rinsing 3 × 10 min in SST with 0.1% TrX, the secondary antibody solution was added. All secondary antibodies were obtained from Jackson ImmunoResearch (Ely, UK) and applied at a dilution of 1:300 for 1 h at room temperature. For detection of the synapsin antibody we used goat anti-mouse IgG conjugated to Cy5 (GAM-Cy5; catalog No. 115-175-166, RRID: AB_2338714). Peptide antibodies raised in rabbit were detected using goat anti-rabbit IgG conjugated to Cy2 or Cy3 (GAR-Cy2; catalog No. 111-225-144; RRID: AB_2338021; GAR-Cy3; catalog No. 111-165-144, RRID: AB_2338006). Following 3 × 10 min rinses in SST with 0.1% TrX, slices were mounted on chrome alum (chromium(III) potassium sulfate)/gelatin-coated microscope slides and dehydrated in an ascending ethanol series (30, 50, 70, 90, 95, 100, 100%; 3 min each). After clearing in xylene (2 × 5 min), slices were embedded and coverslipped using Entellan (Merck, Darmstadt, Germany).

2.5 | Double labeling of allatostatin and FMRFamide in gelatin sections

For double labeling against allatostatin-A and FMRFamide using antisera both raised in rabbit, we prepared brain slices as described above. All following steps were performed at room temperature under agitation. After four 15 min rinses in PBS with 0.3% TrX, slices were preincubated with 5% normal donkey serum (NDS; Jackson ImmunoResearch; catalog No. 017-000-001, RRID:AB_2337254) in SST with 0.5% TrX for 1 h. Next, slices were incubated for at least 18 h with a solution containing the allatostatin-A antiserum (for dilutions of primary antibodies see Table 1), 1% NDS, and 0.5% TrX in SST. Incubation was followed by rinsing 3 × 10 min in SST with 0.1% TrX. All following rinsing steps were carried out in the same way. Next, the rabbit-specific binding sites of the allatostatin antiserum were masked by monovalent, unconjugated goat anti-rabbit Fab fragments (Jackson ImmunoResearch; catalog No. 111-007-003, RRID:AB_2337925) diluted 1:50 in SST and 0.5% TrX for 2 h at room temperature. After another rinsing step, sections were incubated with donkey anti-goat IgG conjugated to Cy3 at a dilution of 1:300 (Jackson ImmunoResearch; catalog No. 705-165-003, RRID: AB_2340411) at room temperature for 1 h. After the next washing steps, sections were incubated with FMRFamide antiserum with 1% NDS, and 0.5% TrX in SST for at least 18 h at room temperature. Following another rinse, slices were incubated with donkey anti rabbit IgG conjugated to Cy2 IgG (1:300; Jackson ImmunoResearch; catalog No. 711-225-152, RRI-D:AB_2340607) for 1 h at room temperature. After rinsing, slices were mounted, dehydrated, cleared, and embedded as described above.

2.6 | Wholemount preparations (peptide staining)

Preparation was identical to the procedures used for gelatin sections, except for the fixative. To facilitate antibody penetration, we fixated in 10% methanol and 4% formaldehyde in 0.01 M PBS overnight at 4°C. After four 15 min rinses in 0.01 M PBS at room temperature, brains were preincubated overnight at 4°C in 5% NGS, 0.3% TrX in 0.01 M PBS with 0.02% sodium azide. Next, the primary antibody solution consisting of the primary antibodies (for dilutions of primary antibodies see Table 1), 1% NGS, 0.3% TrX and 0.02% sodium azide in 0.01 M PBS was applied for 6 days at 4°C. After rinsing 6 × 20 min in 0.01 M PBS with 0.3% TrX at room temperature the secondary antibody solution was applied for 3–4 days at 4°C. It contained the secondary antibodies at a dilution of 1:300, 0.3% TrX, 0.02% sodium azide, and 1% NGS in 0.01 M PBS. This and all subsequent steps were conducted in darkness if possible. After incubation, brains were rinsed 6 × 20 min in 0.01 M PBS with 0.03% TrX and subjected to an ascending ethanol series (25, 50, 70, 90 95, and 100%; 15 min each). After clearing in a 1:1 mixture of 100% ethanol and methyl salicylate for 40 min and in pure methyl salicylate for 40 min, brains were embedded in Permount (Fisher Scientific, Hampton, NH, USA) between two coverslips using eight hole reinforcement rings (Zweckform, Oberlaindern) as spacers.

2.7 | Wholemount preparations (synapsin staining)

Synapsin staining was performed according to a modified version of the protocol from Ott (2008) as described in Hensgen et al. (2020). As for gelatin sections animals were cold anesthetized, waxed to a holder and the head capsule was opened frontally. The brain was covered in HEPES-buffered saline (HBS; 150 mM NaCl, 5 mM KCl, 5 mM $CaCl_2$, 25 mM sucrose, 10 mM HEPES (4-[2-hydroxyethyl]−1-piperazineethanesulfonic acid)) and tissue around the brain was removed. The brains were fixated in the opened head capsule for 1 h with zinc-formaldehyde (18.4 mM $ZnCl_2$, 135 mM NaCl, 35 mM sucrose, 1% formaldehyde; Ott, 2008), then the head was cut off and fixation was continued for 20 h at room temperature. The brains were dissected from the head capsule under HBS, rinsed 8 × 25 min in HBS and 3 × 10 min in TRIS buffer (pH 7.4). After incubation for 85–90 min in 20% dimethyl sulfoxide (DMSO)/80% methanol (Dent's fixative; Dent et al., 1989) brains were rinsed again 3 × 10 min in TRIS buffer. Brains were preincubated overnight at 4°C in 5% NGS in PBSTD (0.01 M PBS with 1% DMSO and 0.3% TrX). Next, brains were incubated for 7–8 days at 4°C with the primary antibody solution containing the antibody against synapsin (see Table 1 for dilutions of primary antibodies), 1% NGS, and 0.02% sodium azide in 0.01 M PBSTD. Following incubation, brains were rinsed 8 × 30 min in PBSTD and subsequently incubated for 8 days at 4°C with the secondary antibody goat anti-mouse IgG conjugated to Cy5 (1:300) with 1% NGS and 0.02% sodium azide in 0.01 M PBSTD. After incubation, brains were rinsed 6 × 30 min in PBSTD and 2 × 30 min in PBS. Brains were dehydrated, cleared, and embedded as described above

except that the 1:1 mixture of 100% ethanol and methyl salicylate was added for 15–20 min and pure methyl salicylate was added for 60 min.

2.8 | Image acquisition and processing

Specimens were scanned using a confocal laser scanning microscope (Leica TCS SP5 or TCS SP8; Leica Microsystems) using either an oil immersion objective (HCX PL APO 20×/0.70 Imm Corr Lbd. bl.), or a 63× glycerin immersion objective (HCX PL APO 63×/1.3 GLY CORR CS 21). Laser lines used for excitation of Cy2/Cy3/Cy5 were provided by the SP5 through an argon laser (488 nm), a diode pumped solid state laser (561 nm) and a helium/neon laser (633 nm), and for the SP8 by diode pumped solid state lasers (488 nm/ 552 nm/638 nm). Multiple chromophores in the same sample were always scanned sequentially. Image stacks were acquired at a scanning frequency of 200 Hz with an *xy*-resolution of 1024 × 1024 pixels at a *z*-step size of 1.5 µm (20× objective) or 0.5 µm (63× Objective). The pinhole was always set to 1 Airy unit.

Confocal stacks were loaded into Amira (version 5.33 or 6.0; Thermo Fisher Scientific Inc., Waltham, MA, USA) and further processed. Optical sections were visualized using the OrthoSlice module.

For 3D-reconstructions, wholemount preparations were scanned with the 20x objective from anterior and posterior at a resolution of 0.75 µm × 0.75 µm × 1.5 µm. The two image stacks were then combined in Amira using the Merge module. Reconstructions of the 3D structure of the CX were made using the segmentation editor. Outlines were drawn in selected sections of the three cardinal orthogonal planes. Using the Wrap function this scaffold was then interpolated to represent a 3D structure. Since the result of this operation usually extends beyond the original neuropil borders, the 3D volume was shrunk by 1 voxel and subsequently smoothed once. Images were exported from Amira as TIFF files and further processed in Photoshop (Adobe Systems, San Jose, USA; RRID:SCR_014199), Photoshop Lightroom (Adobe Systems; RRID:SCR_018012), and Corel Draw (Corel Corporation, Ottawa, Canada; RRID:SCR_014235).

2.9 | Generation of standard average model of the CX

Standardization of the CX, the bulbs, the posterior optic tubercles, and the anterior optic tubercles was carried out on 10 confocal data stacks of antisynapsin labeled wholemount preparations. To prepare the data for the averaging procedure, all voxels in the synapsin stainings that were lying more than 10 voxels outside the 3D-reconstructed areas in the corresponding labelfields were replaced by black voxels using the arithmetic module in Amira. This was necessary to facilitate the registration. The gray values of the remaining voxels in each data set were normalized to a range of 8 bits (256 gray values). The actual standardization was done by applying the iterative shape averaging (ISA) protocol as described by Rohlfing and Maurer (2003) and adjusted by Kurylas et al. (2008), using the computational morphometry toolkit (CMTK, version 3.2.3, RRID:SCR_002234). Voxel counts of the 3D-reconstructed neuropils allowed us to determine the specimen that represented the median neuropil volume of the 10 data sets. This specimen was chosen as the template for the averaging procedure. The choice of the template strongly influences the volume of the averaged data set but has only minor impact on its shape. In the first step of the standardization procedure, the remaining nine data sets were affinely registered onto the template, first using six degrees of freedom (translation and rotation along/around the *x*, *y*, and *z* axes) and then using nine degrees of freedom (additional scaling along the three axes). Next, we calculated the average of each voxel across all 10 data sets (including the template). The result of this operation served as the template for an elastic registration using B-spline free-form deformation model. In this process, a 3D grid is applied to the image stack and the grid nodes are moved to best match the local features of the current brain to the template brain. After applying these calculations to all 10 data stacks, their voxels were averaged, to yield the template for the next elastic registration. This process was carried out seven times in total, with a finer grid in each iteration. The registration parameters from each registration step were stored for each individual data stack and subsequently applied to the corresponding 3D-reconstructions of the neuropils. For each step in the entire registration process, we calculated a shape-based average of the 3D-reconstructions based on signed Euclidean distance maps (Rohlfing & Maurer, 2007). Next, the volume of each neuropil from the averaged 3D-reconstruction was measured and its deviation from the median volume of the 10 original 3D-reconstructions was calculated. For each neuropil, we then identified the registration step that had yielded the average with the lowest volume deviation and used this for the assembly of the shape-based average. For two neuropils, the posterior optic tubercles and the PB (Figure 5), this strategy did not yield sufficiently faithful results with regard to the shape because these brain areas had variable parts, like the tips of the PB (Figure 4). This led to missing voxels in the output like the left posterior optic tubercle, and the left tip of PB (indicated by a white ellipse at bottom left of Figure 6). We therefore repeated the shape-based averaging, this time excluding voxels that were identified as local outliers. A voxel was regarded as an outlier if its distance to the nearest voxel with the same label exceeded a threshold computed from the set of distances over all data sets. Thresholds were calculated as:

$$\text{lower threshold} = Q1 - 1.5 \times (Q3 - Q1)$$
$$\text{upper threshold} = Q3 + 1.5 \times (Q3 - Q1),$$

where $Q1$ and $Q3$ are the first and the third quartile of the distances of all inputs.

Removal of voxels that met the criterion for local outliers yielded more natural shapes for neuropils, that are elongated and variable in shape (posterior optic tubercle, PB), but a more jagged surface for neuropils that are less variable and more spherical in shape (central body neuropils, upper division of anterior optic tubercle). This procedure led to a more symmetric, and hence more representative shape of the PB, which was therefore included into the final average.

2.10 | Central body layers

Layers within the central body neuropils were reconstructed in 3D, based on immunolabeling against four different peptides using Amira software. Borders of layers were defined either by a change in presence or absence of immunolabeling, or by clear changes in the structure of labeled neuronal processes. For better comparison between the layers obtained from different immunostainings, the 3D reconstructions obtained from the different immunostainings were individually registered into the standard average CX. This was achieved by first using the AffineRegistration module in Amira with nine degrees of freedom (rotation, translation, scaling) and subsequently using the warp function in CMTK to perform an elastic registration. To obtain a 3D model that contains all identified layers, we combined the model of the stained FMRFamide layers with the model of the AST layers using the Relabel module in Amira. Individual voxels of the anterior AST-layer in the CBU (I+IIa) that remained on the outside of the FMRFamide layer of the CBU (Ib) after this operation were manually assigned to the FMRFamide layer.

2.11 | Statistical inference

Statistical calculations were computed in Matlab R2021b (The Mathworks, Inc., Natick, MA, USA). To test if the outermost slices of the CBL differ in volume from the other slices, we used the Wilcoxon signed rank test and tested the volumes of each of the two outer slices against each of the inner slices. The significance level of 5% was accordingly adjusted for 14 comparisons using Bonferroni correction.

2.12 | Axes and naming conventions

Body axis rather than neuraxis is used to provide positional information when describing brain structures. Whenever possible, we followed the naming conventions proposed by Ito et al. (2014).

3 | RESULTS

3.1 | General anatomy of the honeybee CX

The CX is situated in the center of the brain and consists of the upper division of the central body (CBU, fan-shaped body in some species), the lower division of the central body (CBL, ellipsoid body in some species), the noduli (NO), and the protocerebral bridge (PB). In the honeybee, the central body is laterally and anterior-ventrally flanked by the pedunculi and the medial lobes (ML) of the mushroom body (Figures 1(a)–1(c) and 1(a′)–1(c′)). The large CBU sits dorsally on the smaller CBL. Its anterodorsal boundary is adjacent to the anterior superior optic tract (ASOT; Figure 1(a); Ehmer & Gronenberg, 2002). The NO are located posterior to the CBL (Figures 1(d), 1(e), 1(d′), and 1(e′)) and are divided into an upper and a lower unit (NOU, NOL; Figures 1(e) and 1(e′)). The large PB is situated between the CBU and the posterior surface of the brain, partly embedded in the cell body rind (Figures 1(f) and 1(f′)). The medial bulb (MBU) and the lateral bulb (LBU), which are not part of the CX but serve as an input station to the CBL, are located laterally to the CBL, immediately posterior to the vertical lobes of the mushroom body (Figures 1(c) and 1(c′)).

The CBL is subdivided into nine wedge-like slices that are clearly separated from each other (Figures 1(a)–1(c) and 2(a) and 2(b)). Volume reconstructions of the nine slices, based on antisynapsin labeling, were made from 10 brains. These reconstructions showed that the outermost slices are considerably shorter in the anterior–posterior axis than all other slices (Figure 2(b)). Consequently, the median volume of each of the outermost slices (28.0×10^3 µm^3) was significantly smaller than the median volume of any of the inner slices (41.3×10^3 µm^3, $p = .98 \times 10^{-3}$ for each of the 14 comparisons of outer against inner columns, Wilcoxon signed rank test with Bonferroni correction, see *Materials and Methods*).

3.2 | Posterior optic tubercle

The posterior optic tubercles (POTUs) are tightly associated with the PB. They are located at the posterior end of the brain between the lateral calyx of the mushroom body and the posterior optic commissure, embedded in the cell body rind (Figures 3(a) and 3(b)). The honeybee POTU is an elongated structure of 80–100 µm length and approximately 30 µm width with a jagged appearance. Its distal end is connected to the PB via a small fiber bundle. The proximal end is tapered. The ventral side of the neuropil has a conspicuous groove (Figure 3(a), arrowhead). Immunostaining with an antiserum against locustatachykinin revealed a strongly stained fiber bundle that runs through this groove to the retrocerebral complex via the Nervus corporis cardiaci II (Figure 3(c), arrowhead). Immunostaining with an antiserum against AST revealed a staining pattern of large varicosities within the POTU (Figures 3(d) and 3(e)). Furthermore, this antiserum labeled a weakly stained, thin fiber connection between the POTUs of both sides of the brain (Figures 3(d) and 3(e) arrowheads). Individual fibers could not be resolved, but the small diameter of this connection suggests that it is made up of a very small number of neurons.

3.3 | Volumetric measurements of the CX and associated neuropils

Volumetric measurements are based on the 10 specimens that were 3D-reconstructed for the standard average (Figure 4 and Table 2). The largest of the reconstructed CX neuropils was the CBU. It had a median volume of 14.5×10^5 µm^3, contributing 62.7% to the total CX neuropil volume (Figure 5(a)). Second and third largest were the PB (4.0×10^5 µm^3, 17.9%) and the CBL (3.1×10^5 µm^3, 13.6%). The smallest CX neuropils were the two NO with a total volume of 1.3×10^5 µm^3, contributing 5.8% to the total CX volume (Figure 5(b)). Of the associated neuropils, the AOTU-UU had the largest median volume (11.9×10^5 µm^3, both sides combined), which also made them

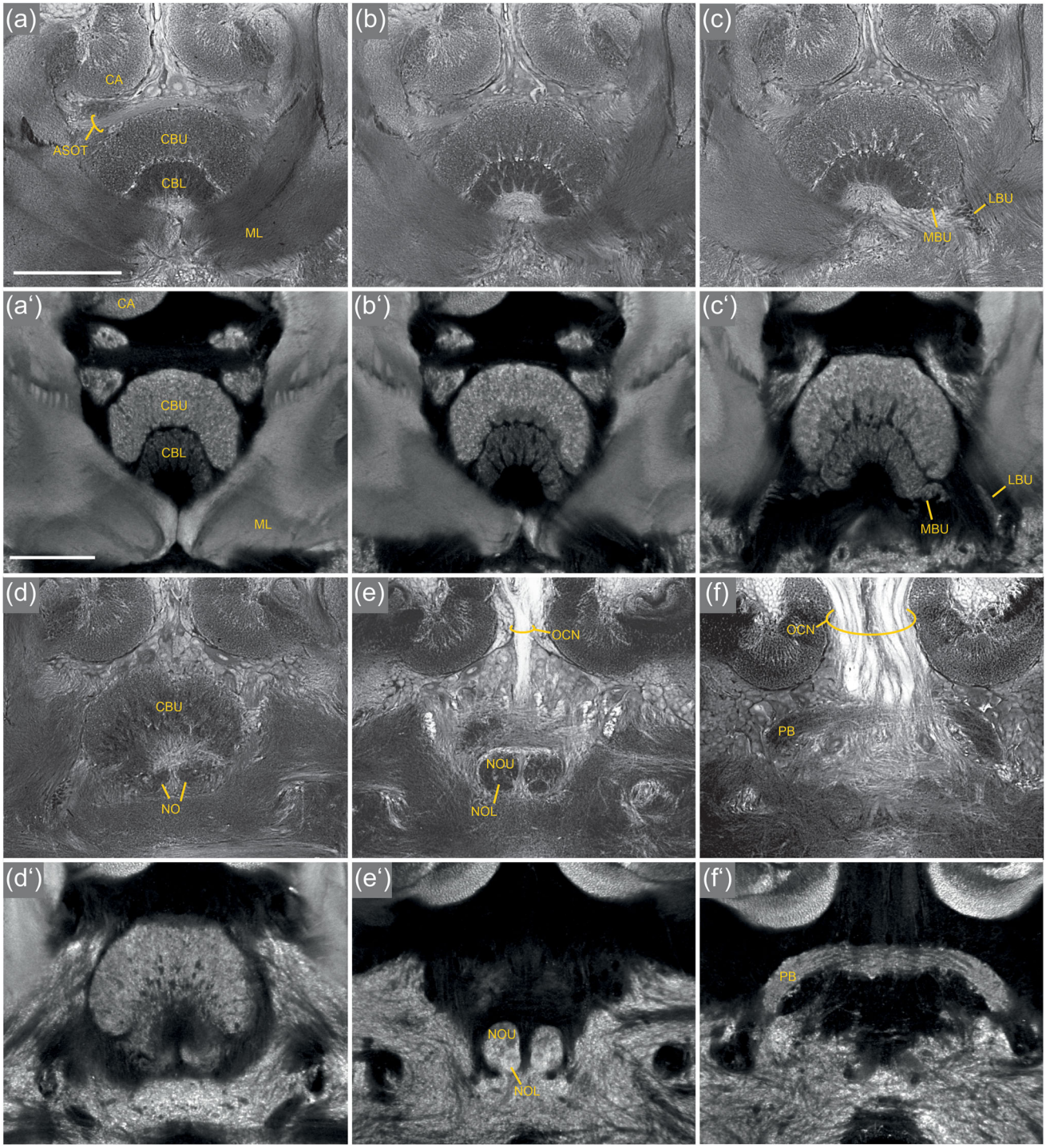

FIGURE 1 Neuroanatomy of the honeybee's central complex in frontal view. (a–f) Osmium contrasted 10 µm sections reveal both neuropils and fibers. (a′–f′) Corresponding optical sections from antisynapsin stained wholemount preparations allow for a better assessment of neuropil structure. (a–c, a′–c′) Sections at different depths in the anterior–posterior axis show the central body upper division (CBU) and the central body lower division (CBL). ASOT, anterior superior optic tract; CA, calyx of the mushroom body; ML, medial lobe of the mushroom body. (d, d′) Posterior aspects of the CBU and anterior parts of the noduli (NO). (e, e′) The NO consists of an upper unit (NOU) and a lower unit (NOU). OCN, ocellar neurons. (f, f′) Protocerebral bridge (PB). Scale bars = 100 µm. Scale bars in (a) and (a′) also apply to (b–f) and (b′–f′), respectively

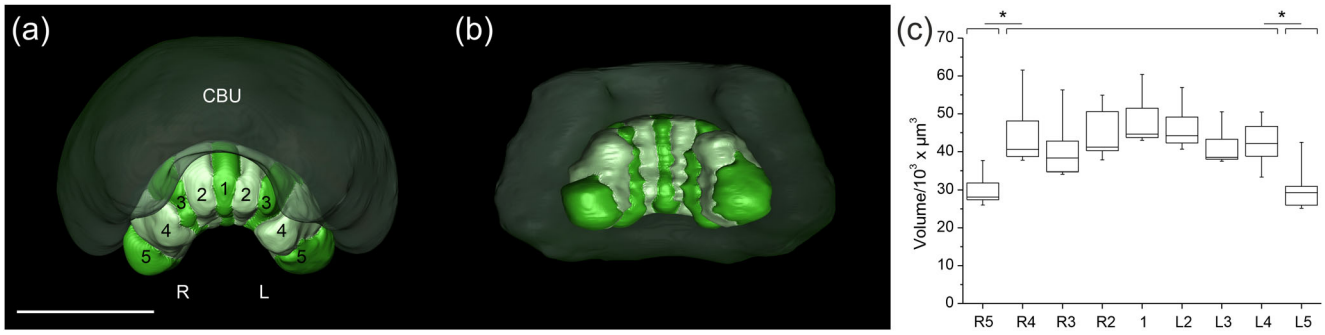

FIGURE 2 Structure and volume of the slices of the lower division of the central body (CBL). (a, b) Surface model of the central body neuropils. (a) Frontal view. The nine slices of the CBL are numbered. R right side of animal; L left side of animal. CBU Central body upper division. (b) Ventral view reveals the shorter anterior–posterior extent of the lateral slices of the CBL. (c) Volumes of the nine individual slices from 10 animals. Upper and lower bound of box signify the 75th and 25th percentile respectively. Horizontal line in box displays the median. Whiskers: 5th and 95th percentile. Asterisks indicate significant differences ($p = .98 \times 10^{-3}$ for each of the 14 comparisons of outer against inner columns, Wilcoxon signed rank test with Bonferroni correction). Scale bar = 100 µm

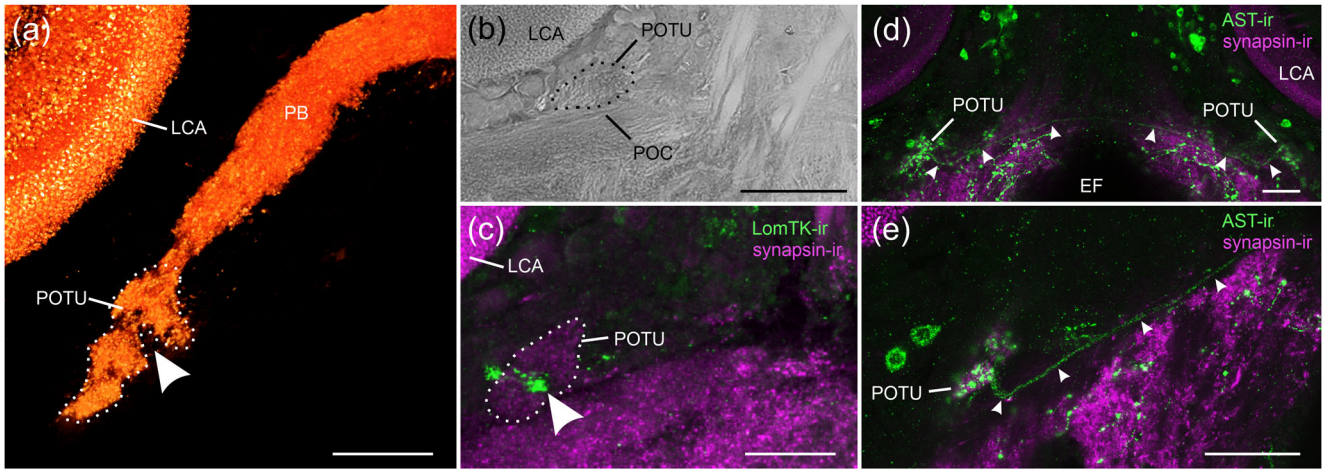

FIGURE 3 Posterior optic tubercle (POTU). (a) Direct volume rendering of antisynapsin staining. The POTU is attached to the protocerebral bridge (PB) through a small fiber bundle. LCA, lateral calyx. Arrowhead points to a groove on the ventral side of the POTU. (b) Osmium-contrasted 10 µm-section shows that the POTU is dorsally and laterally embedded in the cell body rind and that it lies dorsally of the posterior optic commissure (POC). (c) Locustatachykinin-immunoreactivity (LomTK-ir) reveals a fiber bundle that runs through a groove on the ventral side of the POTU (arrowhead) and projects to the retrocerebral complex. (d, e) Allatostatin-A immunoreactivity (AST-ir) reveals varicosities within the POTU and a thin connection between the POTUs on either side of the brain (arrowheads). EF, esophageal foramen. Scale bars = 50 µm

TABLE 2 Volumes of reconstructed neuropils

Neuropil	Median volume (10^5 µm^3)	IQR (10^5 µm^3)	Q1 (10^5 µm^3)	Q3 (10^5 µm^3)	% of CX volume
CBU	14.46	1.05	13.96	15.01	62.7
CBL	3.13	0.40	2.86	3.26	13.6
PB	4.04	0.67	3.61	4.28	17.9
NO	1.30	0.11	1.27	1.38	5.8
AOTU-UU	11.88	1.28	11.43	12.71	NA
AOTU-LUC	1.35	0.26	1.19	1.46	NA
POTU	0.33	0.13	0.23	0.36	NA
MBU	0.36	0.13	0.32	0.45	NA
LBU	0.27	0.13	0.21	0.34	NA

All volumes of paired neuropils are reported as the combined volume of the right and left structure. IQR, interquartile range (Q3–Q1); Q1: 25th quantile; Q3: 75th quantile.

FIGURE 4 Three-dimensional reconstructions of the 10 individual specimens used in this study. Left column: anterior view, right column: posterior view. AOTU-LUC, lower unit complex of the anterior optic tubercles; AOTU-UU, upper units of the anterior optic tubercle; CBL, lower division of central body; CBU, upper division of central body; LBU, lateral bulb; MBU, medial bulb; NO, noduli; PB, protocerebral bridge; POTU, posterior optic tubercle. Scale bar = 150 µm. Interactive 3D-view of specimen #1: https://insectbraindb.org/app/connectomics;experiment=222;handle=EIN-0000222.1

the second largest of all reconstructed neuropils. The other reconstructed neuropils (Figure 5(b)) had volumes of 0.27×10^5 µm^3 (LBU, both sides combined), 0.36×10^5 µm^3 (MBU, both sides combined), 0.33×10^5 µm^3 (POTU, both sides combined), and 1.35×10^5 µm^3 (AOTU-LUC, both sides combined).

3.4 | Standard average

The standard average of the CX and associated neuropils was created using a method based on ISA of antisynapsin staining. The registration process started with an affine registration, followed by seven rounds of elastic registrations with increasingly finer resolution. The results from each iteration are shown in Figure 6. We averaged across 10 specimen and included nine neuropils: CBU, CBL, PB, NO, MBU, LBU, the AOTUs (upper unit and lower unit complex), and the POTUs. The AOTUs were included because TuBu neurons that directly connect to tangential neurons of the CBL (TL neurons, R or ring neurons in *Drosophila*) originate in this neuropil. The posterior optic tubercles were included because they have not been described before in *A. mellifera* and they are connected to the PB via tangential neurons (TB neurons, Δ7 neurons in *Drosophila*) that are an important part of the compass network.

When comparing the volumes of neuropils in the shape-based average after seven iterations of elastic registration to the median volumes of the underlying data set, we noticed that the deviation strongly depended on the absolute size of the respective neuropil. The general trend was that neuropil volume increased at every iteration of the procedure for all neuropils (Figures 6 and 7(a)). In the first registration steps, the number of overlapping voxels between the individual reconstructed specimens was small. Shape-based averaging therefore led to neuropil models that were a lot smaller than the population median. This was especially obvious for small neuropils (Figures 6 and 7(a)). In subsequent iteration steps, larger neuropils reached the population median volume after a few iterations, but smaller neuropils took up to seven iterations. This was also true, when we excluded voxels that were regarded as outliers (Figures 6 and 7(b); for definition of outliers see *Materials and Methods*). The number of iterations needed to obtain the volumes that had the smallest deviation from the median volume of the underlying data set was well described by an exponential decay function (Figure 7(c)). All neuropils with volumes larger than 3×10^5 µm^3, except for the AOTU-UU, reached the best fitting volume after three iterations of elastic registration. To obtain an average 3D-model that is representative of the data set both in shape and in volume, we selected each neuropil from the iteration that resulted in the smallest deviation from the median volume of the data set. This resulted in an average deviation of each neuropil's volume from the median of the underlying data set of only 2.9% (interquartile range: 3.5%; Figure 8).

3.5 | Layers of the central body neuropils

To investigate layering of the central body neuropils, we used antibody stainings against four different peptides: FMRFamide, allatostatin-A, locustatachykinin, and gastrin/cholecystokinin.

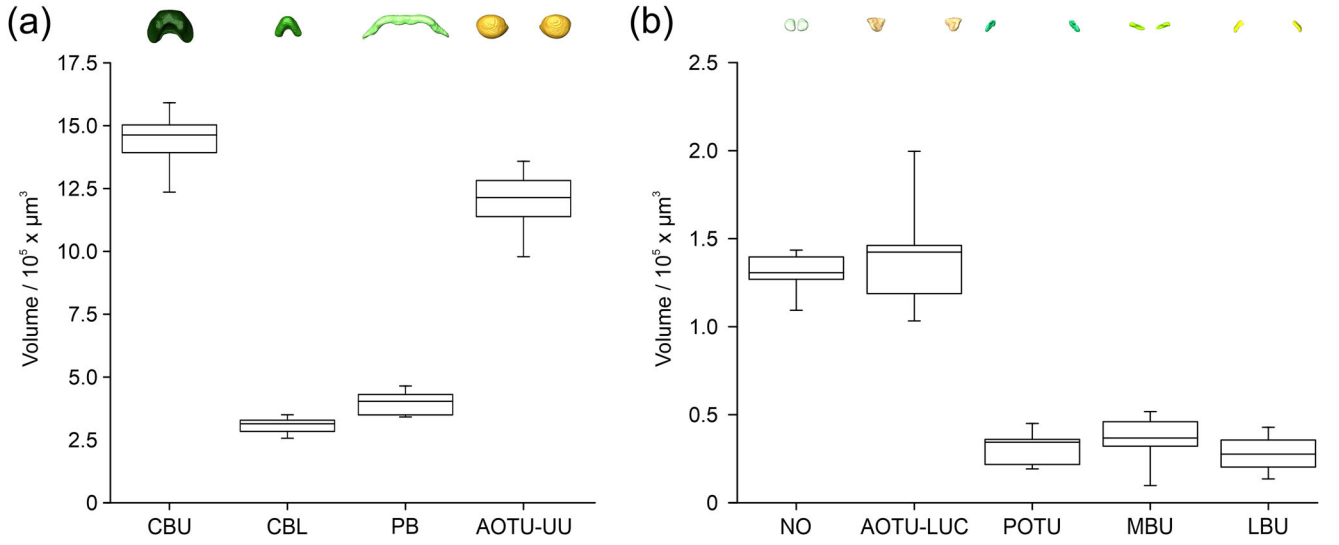

FIGURE 5 Volumes of central-complex compartments and associated neuropils of the 10 specimens that were used in the standard average. Volumes of bilateral neuropils are given as the sum of both sides. (a) Large neuropils. CBU, upper division of central body; CBL, lower division of central body; PB, protocerebral bridge; AOTU-UU, upper units of the anterior optic tubercle. (b) Small neuropils. NO, noduli; AOTU-LUC, lower unit complex of the anterior optic tubercles; POTU, posterior optic tubercles; MBU, medial bulbs; LBU, lateral bulbs

3.6 | FMRFamide immunoreactivity

In the CBU the antiserum against FMRFamide labeled an anterior layer ranging from the dorsal to the ventral edge and spanning roughly a quarter of the anterior-posterior extent of the neuropil (Figure 9(a)). Staining did not extend all the way to the anterior edge of the neuropil and also spared the ventral edge anteriorly, thus revealing a thin anterior/anterior-ventral layer of the CBU (Figure 9(a)). Posterior aspects of the CBU were devoid of immunostaining. The staining had an unusual, conspicuous appearance of irregularly shaped patches (Figures 9(b) and 9(c)). In the CBL, FMRFamide immunolabeling revealed a weakly stained thin layer covering ventral aspects of the neuropil (Figures 9(d) and 9(e)). No staining was observed in the PB or the NO.

3.7 | Allatostatin

Immunoreactivity to the antiserum against *D. punctata* allatostatin I (AST-ir) was abundant in the CX and allowed us to clearly delineate three layers within the CBU and two layers within the CBL (Figure 10(a)). In the CBU, we were able to distinguish between an anterior and a posterior immunoreactive layer enclosing an unstained layer. The staining in the anterior aspects of the CBU consisted of large varicose structures forming a reticulated pattern (Figures 10(b) and 10(c)). In posterior aspects of this layer, the staining was restricted to the dorsal part of the CBU with varicosities that were smaller and more evenly spaced (Figure 10(d)). The posterior layer was innervated by large varicosities (Figure 10(e)). Staining in the CBL revealed a dorsal AST-immunoreactive layer and a ventral AST-immunonegative layer. The fine varicose staining in the CBL stems from tangential neurons that enter the CBL ventrally (Figure 10(d)). The neurites of these neurons run in the isthmus tract and send ramifications through the spaces between the CBL layers into a dorsal layer of the CBL. These neurons are most likely identical to TL5 neurons (Hensgen et al., 2020). Staining in the NO was weak and restricted to their upper part (Figure 10(e)). Strongly stained fibers between the NO and the CBU (Figure 10(e)) and immunoreactivity in the PB (Figure 10(f)) suggest that the staining in the NO stems from CPU4 neurons (Hensgen et al., 2020, PFN neurons in *Drosophila*). The AST antiserum also stained fibers that connect the PB to the AST-immunoreactive processes in the POTU (arrowheads in Figure 10(f)) suggesting the staining of TB neurons (Δ7 neurons in *Drosophila*). AST-ir was also observed in the anterior lip region, which is associated with the CX (Figures 10(g) and 10(g")). To further differentiate the layering revealed by AST-ir, we performed double immunostainings for AST and FMRFamide. As expected from the different appearance of AST-ir and FMRFamide-immunoreactivity (FMRFamide-ir) in the individual stainings, no colabeling of the two peptides was detected. Rather, the two staining patterns were complementary to each other, with the patchy FMRFamide-ir embedded in the reticulated AST-ir pattern (Figure 11). Thus, the FMRFamide-immunoreactive layer corresponds to the reticulated part of the anterior AST-immunoreactive layer (with the exception of the anteriormost and anterior/ventral parts of the AST-ir that are not labeled by the FMRFamide antiserum).

3.8 | Locustatachykinin

Immunoreactivity to the antiserum against *Locusta migratoria* tachykinin II (LomTK-ir) in the CBU was similar to AST-ir showing staining in an anterior and a posterior layer and no staining in

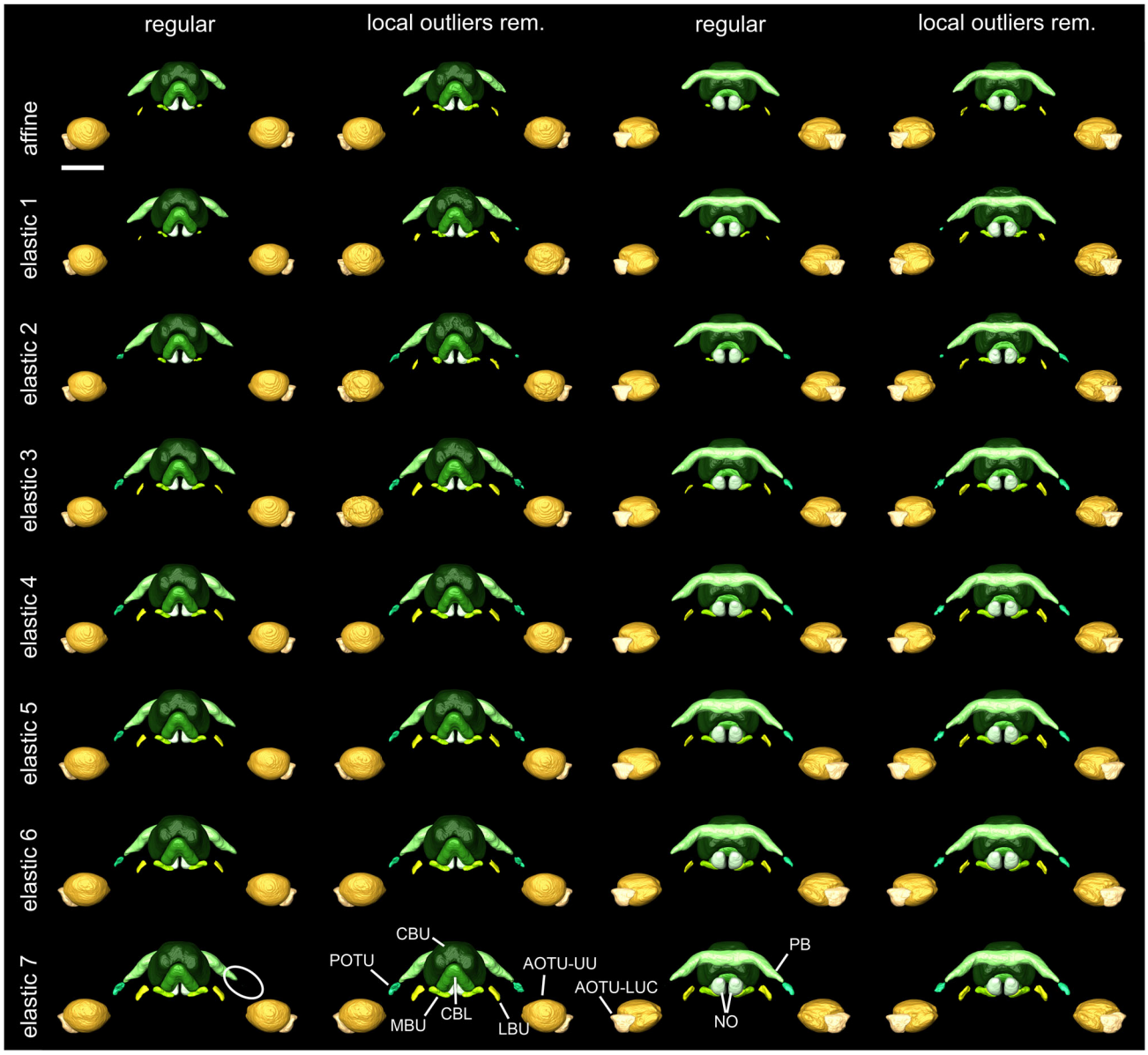

FIGURE 6 Shape-based averages after each iteration of the registration procedure. First row: result of affine registration. Other rows: results of elastic registrations with successively finer grid spacing. Left columns: anterior view. Right columns, posterior view. Shape-based averaging was either done using all voxels (regular) or after removing local outliers (local outliers rem.). For a mathematical definition of local outliers, see *Materials and Methods*. White ellipse at bottom left model indicates missing tip of PB and missing POTU. AOTU-LUC, lower unit complex of the anterior optic tubercles; AOTU-UU, upper units of the anterior optic tubercle; CBL, lower division of central body; CBU, upper division of central body; LBU, lateral bulb; MBU, medial bulb; NO, noduli; PB, protocerebral bridge; POTU, posterior optic tubercle. Scale bar = 150 µm

between (Figure 12(a)). In contrast to AST-ir, the anteriormost and anterior–ventral parts of the CBU remained without staining, similar to FMRFamide-ir. The strongly stained anterior LomTK-immunoreactive layer had a reticulated appearance in its anterior aspects (Figures 12(b) and 12(c)) and evenly distributed varicosities in its more posterior parts (Figures 12(d) and 12(e)) similar to the AST-ir. In contrast to AST-ir, however, the size of the varicosities within this layer was similar in the anterior and posterior part. The posterior layer showed weaker staining with smaller varicosities (arrowheads in Figure 12(e)). The CBL was densely filled with fine granular structures throughout (Figures 12(b)–12(e) and 12(h)). While LomTK-ir did not reveal any layering in the CBL, it clearly revealed the slices of the CBL (Figures 12(c)–12(e)). The NO showed no LomTK-ir (Figure 12(f)). Staining in the PB was weak and consisted of alternating areas with higher and lower density of staining, possibly corresponding to slices of this neuropil (Figure 12(g)).

3.9 | Gastrin/cholecystokinin

Gastrin/cholecystokinin immunoreactivity (GCCK-ir) was confined to an anterior layer in the CBU. Similar to LomTK-ir and FMRFamide-ir,

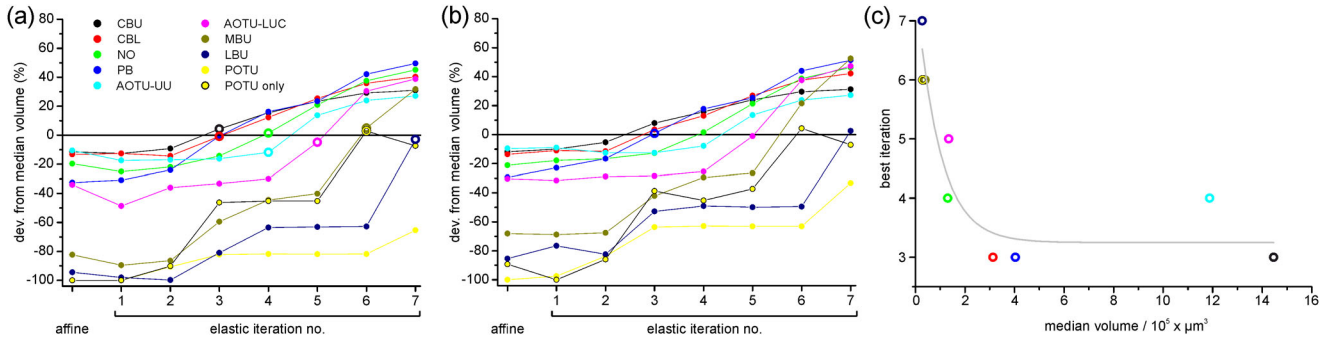

FIGURE 7 Relationship between median neuropil volume and change of 3D-model volume during the registration process. Open circles mark data points that correspond to models used in the final standard atlas. (a) Deviation of the 3D-model volume from median volume of the underlying data set is dependent on the number of iterations of elastic registration. (b) Same as (a), but voxels in individual 3D-models that met the criterion for outliers (see *Materials and Methods*) were excluded from averaging over all 10 models. (c) Number of iterations of elastic registration needed to obtain a 3D-model with a volume that had the smallest deviation from the median volume of the underlying data set, depends on neuropil volume. This relationship was well fitted with an exponential decay function of the form $Y = Y_0 + A \times e^{(-x/d)}$, with Y_0 = offset, A = amplitude and d = decay constant. $Y_0 = 3.2 \pm 0.3$, $A = 4.4 \pm 0.8$, $d = 9.5 \times 10^5 \pm 4.5 \times 10^5$ µm^3, $R^2 = 0.896$

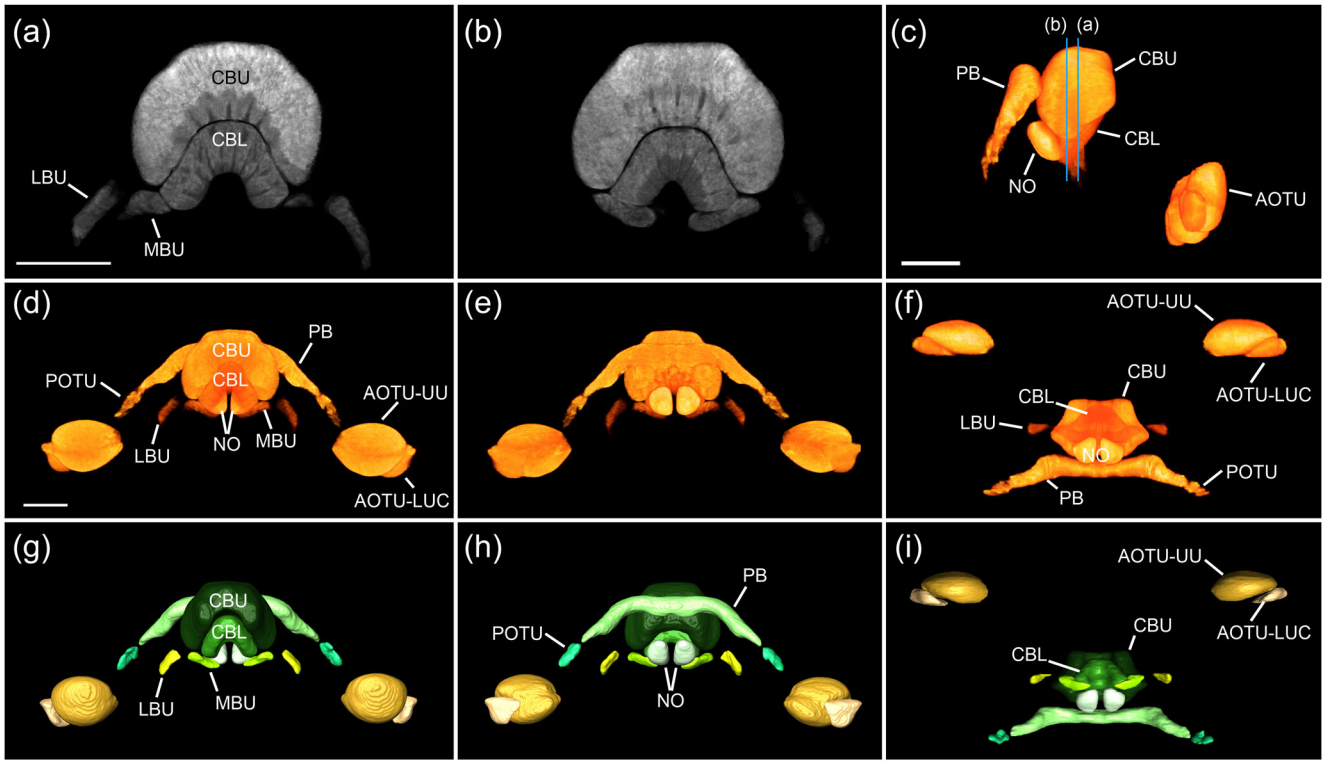

FIGURE 8 Average shape standard atlas of the honeybee central complex and associated neuropiles. (a-f) Averaged antisynapsin staining after seven iterations of elastic registration. (a, b) Frontal optical slices at different depths (indicated as blue lines in (c)). (c–f) Direct volume rendering of averaged antisynapsin grayscale data in lateral (c), frontal (d), posterior (e), and ventral (f) view. (g–i) Shape-based average of 3D-reconstructions in frontal (g), posterior (h), and ventral (i) view. AOTU-LUC, lower unit complex of anterior optic tubercle; AOTU-UU, upper unit of anterior optic tubercle; CBL, central body lower division; CBU, central body upper division; LBU, lateral bulb; MBU, medial bulb; NO, noduli; PB, protocerebral bridge; POTU, posterior optic tubercle. Scale bars = 100 µm. Scale bar in (a) also applies to (b), scale bar in (d) also applies to (e–i). Interactive 3D-view of average shape atlas, including layers shown in Figure 14: https://insectbraindb.org/app/connectomics;experiment=227;handle=EIN-0000227.1

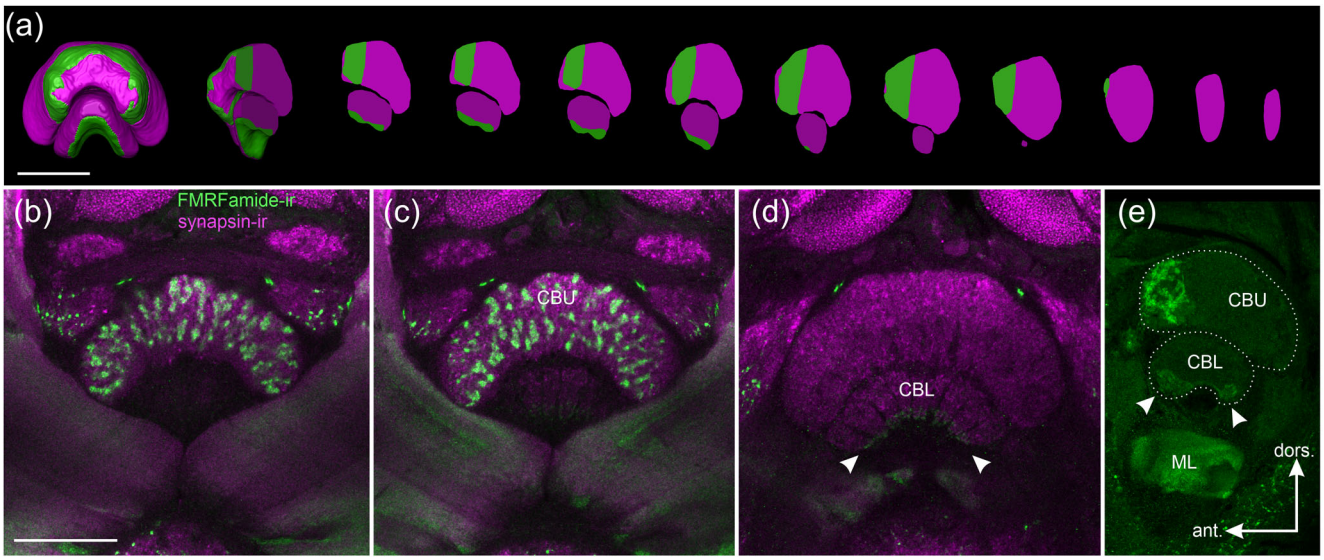

FIGURE 9 Layers in the central body revealed by FMRFamide-immunoreactivity. (a) 3D-model of FMRFamide layers in the central body. From left to right: surface model in frontal view, frontolateral view of sagittally cut surface model, sagittal slices through 3D-model from medial to lateral. Green: FMRFamide positive layers, magenta: FMRFamide negative layers. (b–d) Frontal confocal images of FMRFamide- and synapsin-immunostained gelatin sections at different planes from anterior to posterior. (e) Sagittal confocal image of FMRFamide-immunostained gelatin section. Arrowheads in (d) and (e) indicate weakly stained layer in the central body lower division (CBL). CBU, central body upper division; ML, medial lobe of the mushroom body. Scale bars = 100 µm. Scale bar in (b) also applies to (c–e). Interactive 3D-view of model shown in (a): https://insectbraindb.org/app/connectomics;experiment=235;handle=EIN-0000235.1

GCCK-ir was not found in the anteriormost and anterior/ventral aspects of the CBU. In addition, a small anterior dorsal part remained unstained as well (Figure 13(a)). Staining in the CBU was weak and consisted of medium sized varicosities. The CBL was densely filled with small, intensely stained varicosities (Figures 13(b)–13(e) and 13(h)). Owing to a lack of staining between the slices of the CBL, the slices became clearly visible in this staining (Figures 13(b)–13(e)). Like anti-LomTK, labeling the PB was rather weak and revealed a stripe-pattern of alternating staining densities. The clear visibility of slices in the PB and the CBL indicates that the GCCK antiserum labels columnar neurons in these neuropils. Staining of neurites between the CBL and the PB (Figure 13(g) arrowheads) suggest that these neurons correspond to CL1 neurons (Hensgen et al., 2020; EPG/PEG neurons in *Drosophila*).

3.10 | Inclusion of layers into CX-atlas

By comparing the layers identified in the four antipeptide immunostainings (Figure 14(a)) we were able to define a total of five layers in the CBU and three layers in the CBL (Figures 14(b) and 14(c)). In the CBU, we defined an anterior layer consisting of two sublayers (CBU-Ia and CBU-Ib), a medial layer consisting of two stacked sublayers (CBU-IIa and CBU-IIb) and a posterior layer (CBU-III). In the CBL a dorsal layer (CBL-I) and a ventral layer consisting of two sublayers (CBL-IIa and CBL-IIb) were defined. In the CBU, layer Ia was only stained by the AST antiserum. Layer Ib was stained by all four antisera and corresponds to the patched or reticulated area. Layer IIa was stained by all antisera except the one raised against FMRFamide, while layer IIb remained unstained in all preparations. Layer III was stained by the antisera against AST and LomTK. In the CBL, layer information could only be extracted from the stainings for AST and FMRFamide, where layers I and IIb were stained, respectively. Antisera against LomTK and GCCK stained all CBL layers.

4 | DISCUSSION

We created a standard average 3D atlas of the honeybee CX and associated neuropils using a new approach, based on ISA. We demonstrate that in the iterative standardization process, the number of iterations that yields the best match between the neuropil volumes in the final standard and the data set is different for each neuropil. It depends mostly on the absolute size of the neuropil and, to a lesser degree, on its shape. By choosing each neuropil from the iteration that gives the best matching volume, we obtained a standard average, that is both faithful in shape and in volume. To obtain an even more detailed reference model, we then registered 3D-models of central body layers, obtained from immunostainings against four different peptides to that reference and were able to identify five layers in the CBU and three layers in the CBL.

4.1 | Standardization procedure

The ISA procedure was originally developed to create platforms that allow registration of individual reconstructed neurons from different individuals and was first applied to the honeybee brain (Brandt et al., 2005; Rohlfing et al., 2001). After an initial affine registration

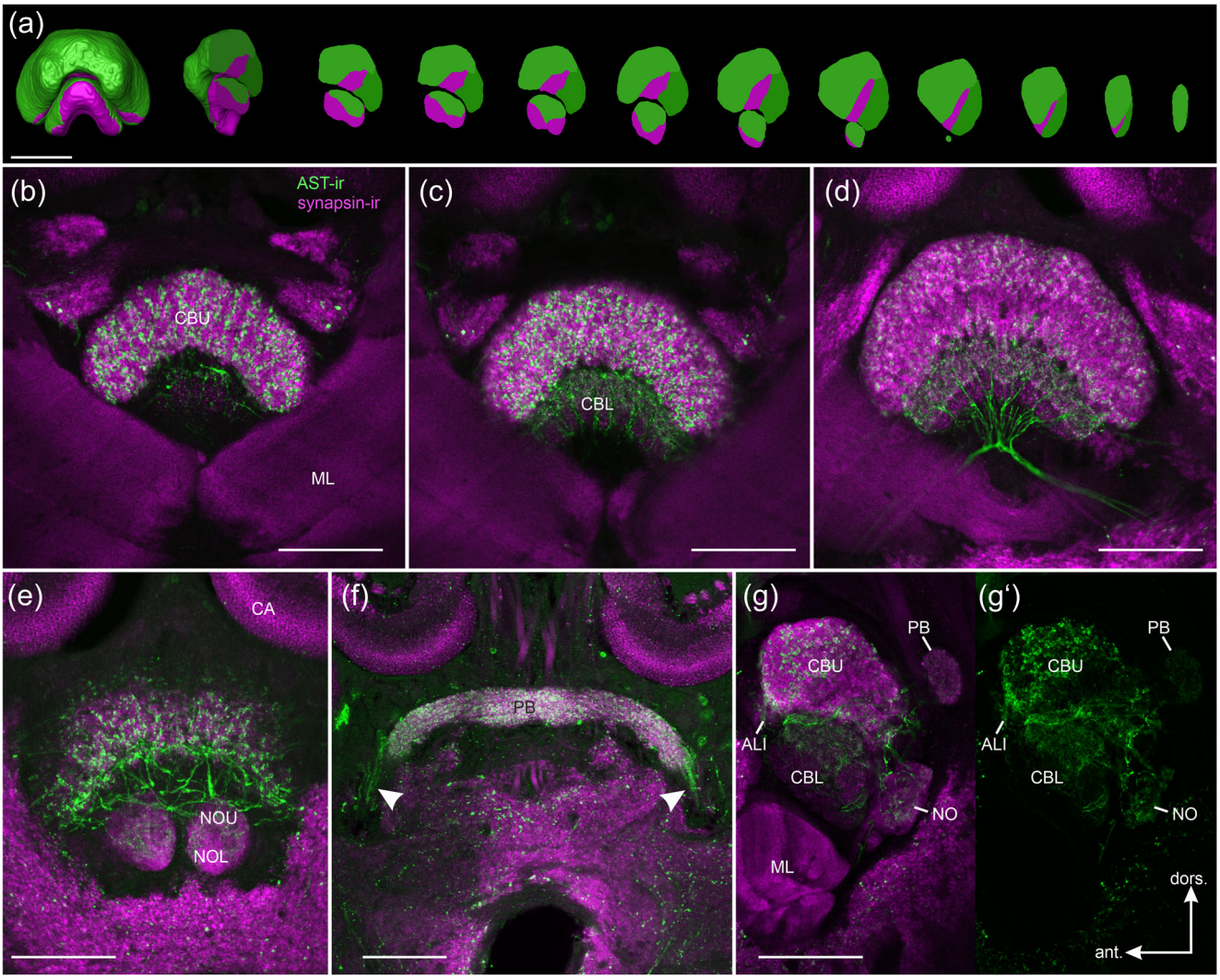

FIGURE 10 Layers in the central body revealed by allatostatin-A (AST) immunoreactivity. (a) 3D-model of AST layers in the central body. From left to right: surface model in frontal view, frontolateral view of sagittally cut surface model, sagittal slices through 3D-model from medial to lateral. Green: ASTpositive layers, magenta: AST-immunonegative layers. (b–f) Frontal confocal images of AST- and synapsin-immunostained gelatin sections at different planes from anterior to posterior. (f) Arrowheads indicate fibers from the PB running towards the POTU. (g, g′) Sagittal confocal image of AST-immunostained gelatin section. ALI, anterior lip; CBL, central body lower division; CBU, central body upper division; ML, medial lobe of the mushroom body; NOL, nodulus lower unit; NOU, nodulus upper unit. Scale bars = 100 µm. Interactive 3D-view of model shown in (a): https://insectbraindb.org/app/connectomics;experiment=234;handle=EIN-0000234.1

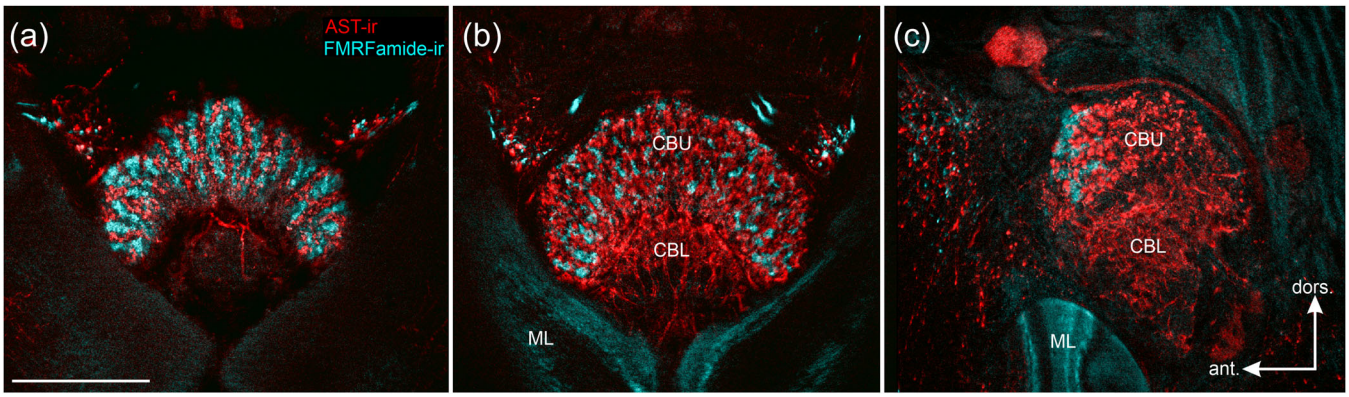

FIGURE 11 Double immunostaining for allatostatin-A (red) and FMRFamide (cyan). (a, b) Frontal view at different depths. (c) Sagittal view. CBL, central body lower division; CBU, central body upper division; ML, medial lobe of the mushroom body. Scale bar = 100 µm. Scale bar in (a) also applies to (b and c)

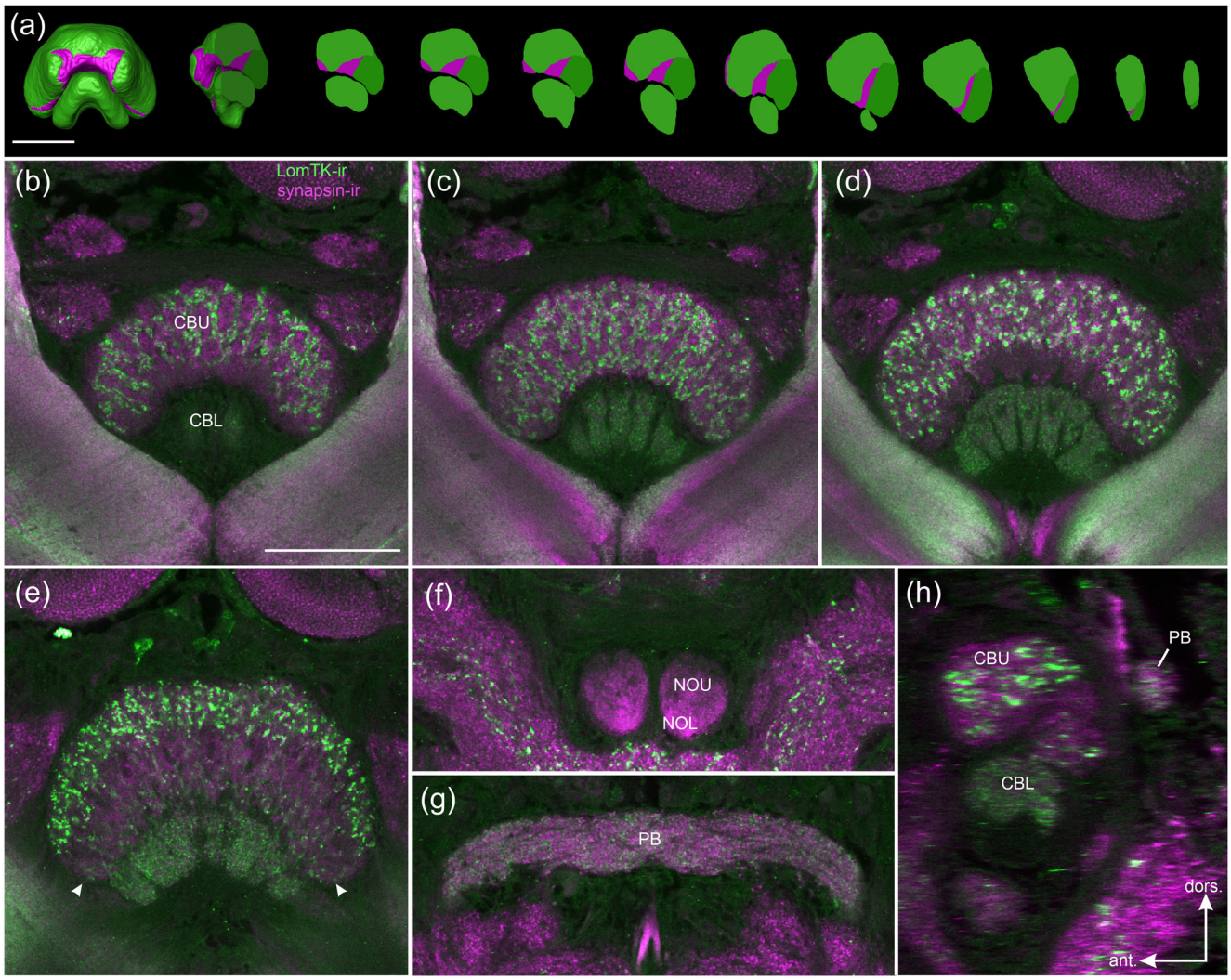

FIGURE 12 Layers in the central body revealed by locustatachykinin-immunoreactivity. (a) 3D-model of locustatachykinin layers in the central body. From left to right: surface model in frontal view, frontolateral view of sagittally cut surface model, sagittal slices through 3D-model from medial to lateral. Green: tachykinin positive layers, magenta: locustatachykinin negative layers. (b–g) Frontal confocal images of tachykinin- and synapsin-immunostained gelatin sections at different planes from anterior to posterior. (h) Sagittal optical section of confocal image from locustatachykinin-immunostained wholemount preparation. CBL, central body lower division; CBU, central body upper division; NOL, nodulus lower unit; NOU, nodulus upper unit; PB, protocerebral bridge. Scale bars = 100 µm. Scale bar in (b) also applies to (c–h). Interactive 3D-view of model shown in (a): https://insectbraindb.org/app/connectomics;experiment=237;handle=EIN-0000237.1

interindividual differences are removed through iterative elastic registration and averaging, and a smooth final average is obtained (Kurylas et al., 2008). The ISA protocol is optimized to obtain the best spatial representation of the neuropils in the model, but not for faithful representation of the neuropil volume, for which the virtual insect brain (VIB) protocol was developed (Jenett et al., 2006). For the locust standard brain, Kurylas et al. (2008) showed that the models created using the ISA method have a better spatial representation of the neuropils and their relative position than models created by the VIB method, but are less accurate in volume. It also becomes clear from their data, that the deviation between the volumes of the standard brain atlas and the underlying data set using the ISA protocol is larger in the smaller neuropils, which is consistent with observations presented in this paper. While the accurate spatial representation of neuropils is an important feature of average shape atlases, it is also desirable that neuropil volumes match the population median as closely as possible. This is important for two reasons. First, the better the volumetric match to the population median, the smaller the average deformation that is needed when registering individual data sets onto the standard. Second, a proper volume representation of all neuropils in the atlas allows it to be used for volumetric comparison with individual brains, for example, in plasticity studies.

Our method achieves volume fidelity by assembly of the final standard atlas from the iterations in the ISA procedure that yield the best volumetric representation of the neuropil, resulting in a median deviation between the final standard atlas and the median of the

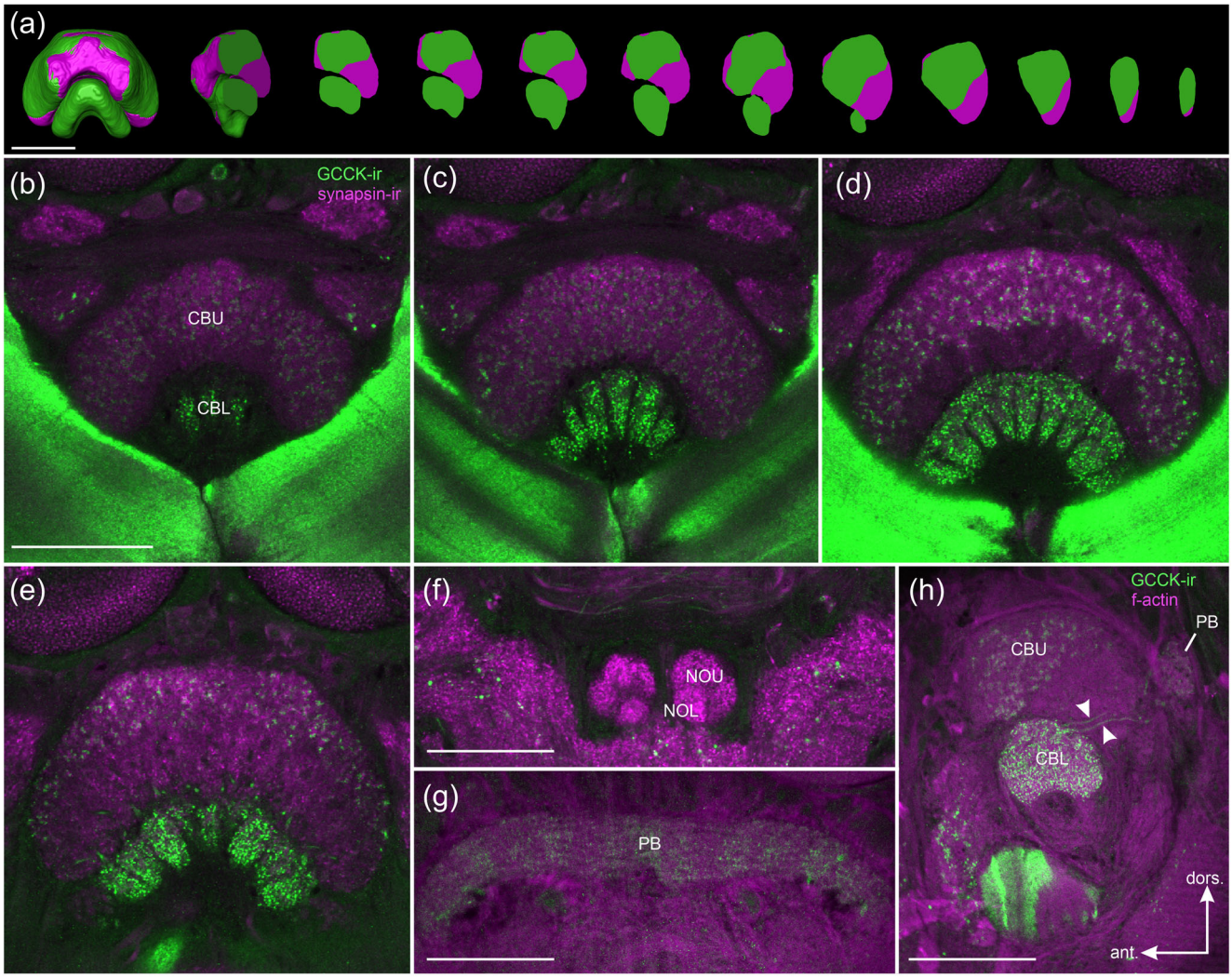

FIGURE 13 Layers in the central body revealed by gastrin/cholecystokinin-immunoreactivity. (a) 3D-model of gastrin/cholecystokinin layers in the central body. From left to right: surface model in frontal view, frontolateral view of sagittally cut surface model, sagittal slices through 3D-model from medial to lateral. Green: gastrin/cholecystokininpositive layers, magenta: gastrin/cholecystokinin-immunonegative layers. (b–g) Frontal confocal images of gastrin/cholecystokinin- and synapsin-immunostained gelatin sections at different planes from anterior to posterior. (h) Sagittal confocal image of gastrin/cholecystokinin-immunostained gelatin section. Arrowheads indicate neurites of CL1 (EPG/PEG) neurons. CBL, central body lower division; CBU, central body upper division; NOL, nodulus lower unit; NOU, nodulus upper unit; PB, protocerebral bridge. All scale bars = 100 µm. Scale bar in (b) also applies to (c–e). Interactive 3D-view of model shown in (a): https://insectbraindb.org/app/connectomics;experiment=236;handle=EIN-0000236.1

underlying population of only 2.9%. For comparison we calculated the median deviation between the neuropil volumes in the average shape atlas and the mean volumes of the underlying data set for four other species: the desert locust (16.0%; Kurylas et al., 2008), the madeira cockroach (3.0%; Wei et al., 2010), the jewel wasp (9.1%; Groothuis et al., 2019), and the bumblebee (14.6%; Rother et al., 2021). In all cases, except for the cockroach the deviation was three to five times higher than the value reported here. It is unclear, why the deviation is small for the cockroach, despite the use of the standard procedure. It is unlikely that larger sample size (n = 20) in comparison with the jewel wasp and bumblebee is the reason, because locust standard brain is also based on 20 specimens. It is not clear if the number of voxels plays a role because total voxel number was not reported for the cockroach. However, between the locust and the bumblebee standard brain, voxel numbers are higher for the locust, but volume deviation is higher. Possibly the variation between the individual specimen was lower for the cockroach than for the other species. While under unknown circumstances, it seems possible to achieve high volume fidelity using the standard ISA method, our new approach offers a straightforward and reliable method for significant improvement of the volume fidelity of ISA-based standard atlases.

It should be noted, however, that our new procedure might not be applicable to all data sets. In cases where two neuropils are in close proximity to each other, using neuropil models from different iterations

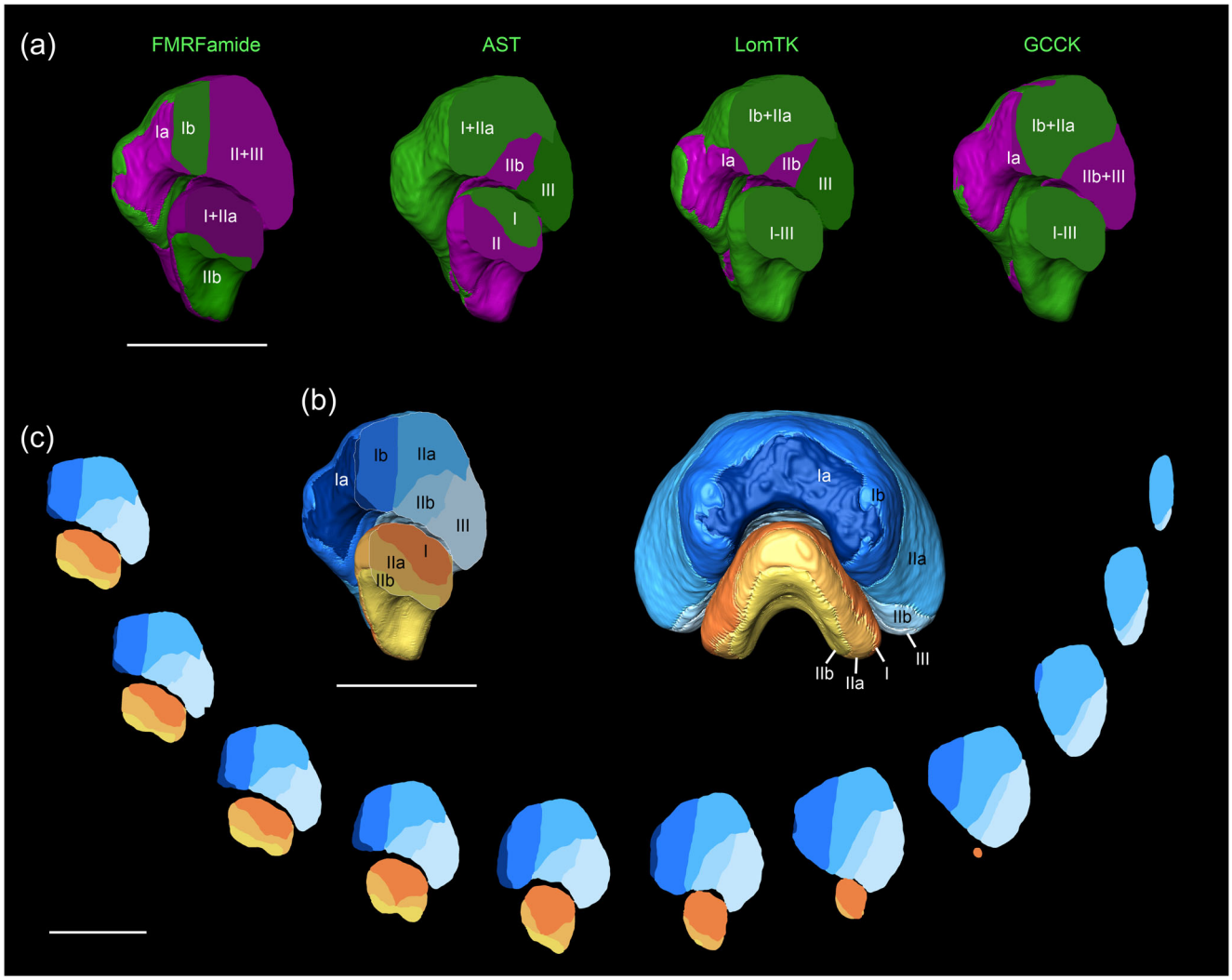

FIGURE 14 Summary of central body layers. (a) Summary of layers identified by antibody stainings. (b) Central body 3D-model comprising all layers identified in this study. Left: oblique view of surface model sagittally sliced in the middle. Right: frontal view of surface model. Shades of blue: CBU. Shades of orange and yellow: CBL. (c) Sagittal planes of 3D-model from medial to lateral. Scale bars = 100 µm. Interactive 3D-view of average shape atlas, including layers and neuropils shown in Figure 8: https://insectbraindb.org/app/connectomics;experiment=227;handle=EIN-0000227.1

for the assembly of the final standard might lead to overlapping voxels. This is especially likely, when the volume deviation of the neuropils used is positive, that is, when they are larger than the corresponding values of the population. In such cases, there would be two possible compromises that could be made. (1) If the priority lies on shape fidelity, one could use the neighboring neuropil from the iteration that delivers the second-best volume fit and results in no overlapping voxels. (2) If volume fidelity is more important, the overlapping voxels could be assigned to either of the two neuropils, if a good argument can be made to do so.

4.2 | Posterior optic tubercle

The POTU has been identified in a variety of insect species, including the desert locust (Würden & Homberg, 1995), the cockroach *R. maderae* (Stengl & Homberg, 1994), the jewel wasp *Nasonia vitripennis* (Groothuis et al., 2019), and three lepidopteran species (*Danaus plexippus*: Heinze & Reppert, 2012; *Helicoverpa armigera*: Tang et al., 2019; *Agrotis infusa*: Adden et al., 2020), but seems to be lacking in *Drosophila* (Wolff et al., 2015) and dung beetles (el Jundi et al., 2018). In honeybees, an anatomical description of the POTU was so far lacking, but it has been previously shown that fibers, which show immunoreactivity to pigment dispersing factor (PDF-ir) branch in and around this neuropil (Beer et al., 2018). This suggests that circadian information is combined with compass information at this stage, which might contribute to the time compensation of the honeybee's sky compass. A similar connection has been shown in the desert locust, where the POTU has been investigated in some detail (Homberg & Würden, 1997). An ultrastructural study demonstrated that PDF-ir is found in fibers that have output synapses in the POTU (Held et al., 2020), suggesting that the POTU in locusts receives direct input from the accessory medulla.

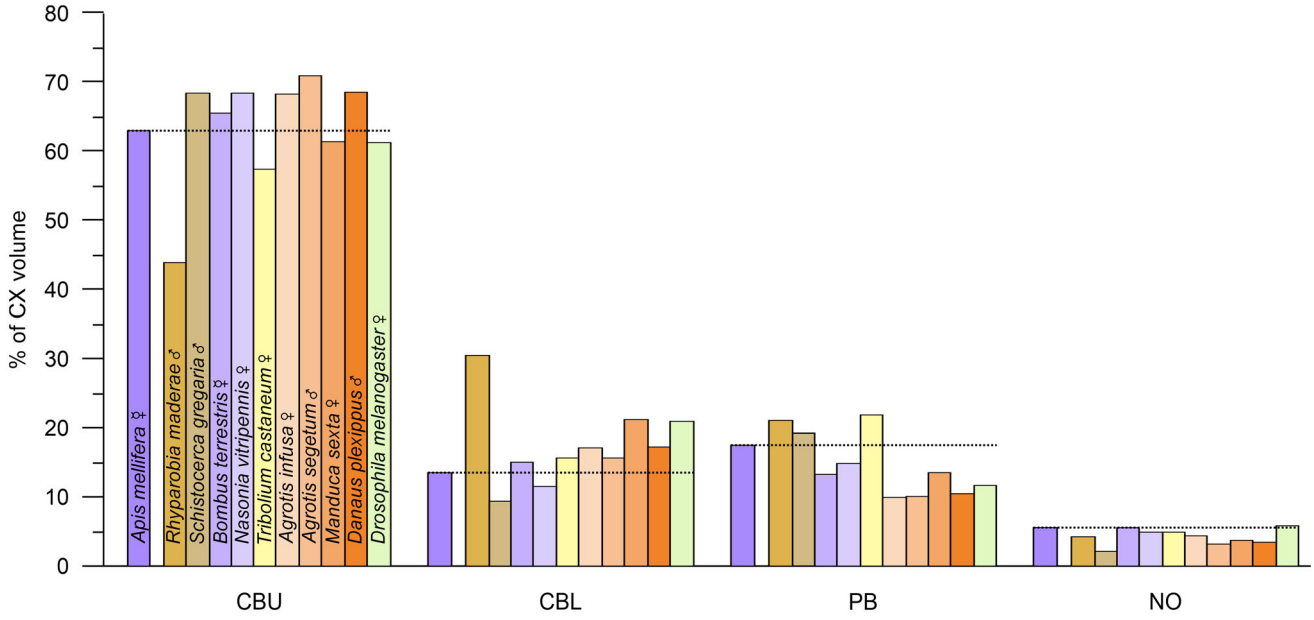

FIGURE 15 Comparison of relative volumes of the compartments of the central complex in different species. Horizontal lines indicate relative volume in *Apis* (from this study). Shades of purple: Hymenoptera, shades of brown Polyneoptera, yellow: Coleoptera, orange: Lepidoptera, green: Diptera. Data compiled from Wei et al. (2010) (*R. maderae*), Kurylas et al. (2008) (*S. gregaria*), Rother et al. (2021) (*B. terrestris*), Groothuis et al. (2019) (*N. vitripennis*), Dreyer et al. (2010) (*T. castaneum*), Vries et al. (2017) (*A. segetum*), Adden et al. (2020) (*A. infusa*), el Jundi et al. (2009) (*M. sexta*), Heinze et al. (2013) (*D. plexippus*), Rein et al. (2002) (*D. melanogaster*).

As in the honeybee, the locust POTU is therefore assumed to play a role in time-compensation of the sky-compass. Intracellular recordings demonstrated that tangential neurons of the PB with branches in the POTU represent preferred directions of polarization in the slices of the PB and additionally respond to an artificial sun stimulus (Heinze & Homberg, 2007; Pegel et al., 2018; Pegel et al., 2019). It has further been shown that the POTUs of both brain hemispheres are connected through polarization-sensitive interneurons (pTuTU neurons; el Jundi & Homberg, 2010). This connection has been speculated to stabilize the polarotopic layout of the PB (Beetz et al., 2015). In the honeybee, we found a similar bilateral connection that showed AST-ir (Figures 3(c) and 3(d)) underlining a high degree of conservation of the CX network, even between distantly related species.

4.3 | Comparison with volumetric data from other species

To compare our volumetric data with that obtained in other insect species, we compiled a list of relative volumes of the CBU, CBL, PB and NO from eleven species across six insect orders, including the honeybee (Figure 15). Relative volume of the CBU ranges between 44% in *Rhyparobia maderae* and 71% in *Agrotis segetum*. The honeybee ranges approximately in the middle with 63% (neglecting the extreme value of *R. maderae*). For the CBL of the holometabolous species, the range was between 12% in *Nasonia vitripennis* and 21% in *Manduca sexta and Drosophila melanogaster*. Along with the two other Hymenopteran species, the bee ranges at the lower end of the spectrum (14%), while the hemimetabolous species hold the extreme values (*R. maderae*: 31%, *Schistocerca gregaria*: 10%). Relative volumes of the PB range between 10% (*Agrotis infusa*) and 22% (*Tribolium castaneum*). The relative volume of the honeybee's PB is at the upper end of the range (18%) and the largest of the three Hymenopteran species. Relative volumes of the noduli range between 2.2% (*S. gregaria*) and 5.9% (*D. melanogaster*). The relative volume of the honeybee's NO ranged at the upper end (5.7%).

4.4 | Layers of the central body

We provide the first detailed 3D-analysis of layers in the honeybee CX. While immunostaining for AST-A, FMRFamide, LomTK II, and GCCK have been done in the honeybee brain before, the focus of these reports was not on the CX or its layers (AST: Kreissl et al., 2010, FMRFamide: Schürmann & Erber, 1990; Strausfeld et al., 2000, GCCK: Strausfeld et al., 2000, LomTK II: Galizia & Kreissl, 2012). The layers defined in this work are based on the combination of results from different immunostainings. Some of the individual layer boundaries were identified across different immunostainings. This suggests that the neuropil borders identified by these stainings are not merely a neuroanatomical feature but define functional units of the CX. Multiple examples from *Drosophila* show that anatomically defined layers in the CX are linked to specific functions (e.g. Hardcastle et al., 2021; Hu et al., 2018; Liu et al., 2006; Weir & Dickinson, 2015; Xie et al., 2019). In the honeybee, a lack of electrophysiological data precludes the attribution of specific tasks so far. The identity of the layers defined here

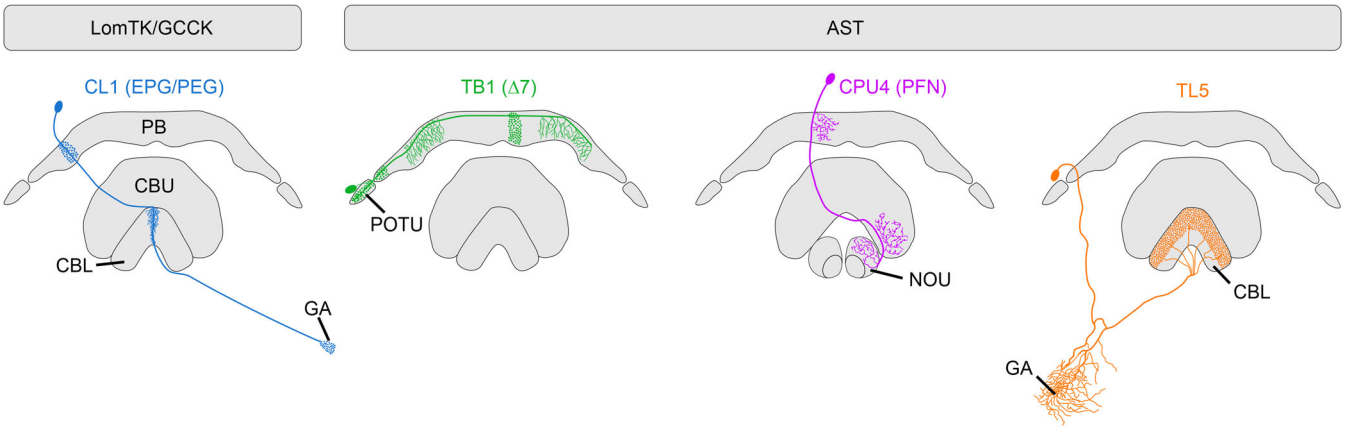

FIGURE 16 Summary of immunocytochemically identified neuronal cell types. Schematic drawing shows CL1 neurons, that were labeled by LomTK and GCCK antisera and three types of neuron labeled by the AST antiserum (TB1, CPU4, and TL5). Abbreviations in brackets indicate names of the corresponding neurons in *Drosophila*.

is also supported by other reports of immunostainings in the honeybee CX, where some of the layers presented here have been identified. Most notably layer CBU-Ib can be readily identified due to its unusual patchy staining pattern (Figures 9 and 11). Such a pattern has been previously reported in Acetylcholinesterase staining (Kreissl & Bicker, 1989), immunolabeling of dopamine (Schäfer & Rehder, 1989), and tyrosine hydroxylase (Timm et al., 2021). Tyrosine hydroxylase staining labels the three main layers of the CBU (I, II, III), but does not allow to distinguish the sublayers (a, b). In the CBL, tyrosine hydroxylase-ir is mostly found in a dorsal layer probably corresponding to CBL-I (Timm et al., 2021). A similar threefold layering of the CBL as reported here seems to emerge from immunolabeling of the tyramine receptor AmTAR1, which labels the CBL layers I and IIb (Timm et al., 2021).

4.5 | Comparison with layers defined by neuron type and functional implications

One major function of the CX is to serve as an internal navigation system by coding head direction, movement direction and producing output commands necessary for goal directed motor responses (Lu et al., 2022; Lyu et al., 2022; Pfeiffer & Homberg, 2014; Seelig & Jayaraman, 2015). Immunohistochemistry allowed us to identify four types of neuron of the CX circuitry based on characteristic ramifications and branching patterns (summarized in Figure 16). LomTK and GCCK stained CL1 neurons (EPG/PEG neurons *Drosophila*). The exact subtype could not be determined from the stainings. EPG neurons are a core element of the ring-attractor network in in the CX and hold a representation of current head direction of the animal with respect to an external frame of reference (Seelig & Jayaraman, 2015; Stone et al., 2017). In locusts, a subset of CL1 neurons has also been shown to be immunoreactive to the locustatachykinin II antiserum (Vitzthum & Homberg, 1998). This is noteworthy, because the distribution of LomTK-ir, like that of other neuropeptides is rather variable between species (Vitzthum & Homberg, 1998). AST-ir allowed us to identify three types of neuron in the CX: TB (Δ7 in *Drosophila*), CPU4 (PFN in *Drosphila*) and TL5. Both TB and CPU4 neurons are an integral part of the compass network. In locusts, TB neurons have been shown to hold a representation of the animal's head direction with respect to polarized light (Heinze & Homberg, 2007). Newer work in *Drosophila* shows that these neurons are essential to the compass-network, as all neurons downstream of EPG neurons that carry a heading signal receive input from Δ7 neurons (Hulse et al., 2021). One type, to which this applies are CPU4 neurons (PFN in *Drosophila*). CPU4 neurons receive an optic flow signal in the NO, a heading signal in the PB and project to the CBU. In a computational model for path integration, these neurons have been speculated to carry a memory signal for the home vector (Stone et al., 2017). Work in *Drosophila* shows that subsets of these neurons play an important role in transforming the heading signal from body-centric to world-centric coordinates (Lu et al., 2022; Lyu et al., 2022). In bumblebees, it was shown that PFN neurons are the most abundant columnar cell type in the CX with a total count of 854 (Sayre et al., 2021). As in CL neurons, where isomorphic sets of neurons can be distinguished by their peptide- or transmitter content, the AST antiserum labels only a subset of these neurons. Kreissl et al. (2010) counted 70 AST-positive cell bodies in the PI, which likely belong, at least in part, to the CPU4 neurons. The third neuronal cell type labeled by the AST antiserum were TL5 neurons, which were identified by their conspicuous branching pattern (Hensgen et al., 2020).

In a previous study, targeting neuronal cell types in the honeybee CX, we have identified some of the layers described here based on staining of individual neurons or groups of neurons through electroporation (Hensgen et al., 2020). It should, however, be noted that this does not necessarily mean that the neurons mentioned in the following are stained by the antisera used to identify the respective layers. A layer that corresponds to layer CBU-I was identified based on staining of pontine neurons (PoU). These neurons are intrinsic to the CBU and connect two slices, one in each hemisphere and eight slices apart. According to the nomenclature of Sayre et al. (2021) in bumblebees, these neurons would be called hΔ type 6. A subtype of pontine

neurons in *Drosophila*, called hΔB has recently been shown to signal the allocentric travelling direction, that is, the direction, in which the body moves, irrespective of head direction (Lu et al., 2022; Lyu et al., 2022). It is, however, not clear if these neurons are homolog to PoU neurons in the honeybee. Columnar neurons of the CBU (CPU1 and 2) were restricted to posterior aspects of the CPU. While the branching areas of CPU1a type 2 neurons seem to be identical to CBU layer III, those of the other CPU neuron types were not clearly consistent with the layers described here, indicating that there might be further subcompartments in the CBU. CPU1/2 neurons (PFL1, 2, and 3 in *Drosophila*) are regarded as the output stage of the compass system (e.g., Heinze & Homberg, 2008; Hensgen et al., 2020), therefore layer III and possibly parts of layer IIa are likely to be the areas where the last processing steps before the premotor output take place. This idea is further strengthened by ramifications of tangential TUVES2 neurons in the same areas which have been proposed to receive input in the superior intermediate protocerebrum (SIP) and send output to the lateral complex. These neurons belong to the largest groups of neurons described from the CBU of honeybees: tangential neurons or TU neurons. Some ramification patterns of TU neurons clearly matched the layers defined here (e.g., TUPI1: layers I/IIa; TUVES2, TUSLP2: layer3). Based on the light microscopic appearance of their branches, many of the TU neurons receive input in the superior neuropils (superior lateral, superior intermediate and superior medial protocerebrum, SLP, SIP, SMP). In *Drosophila*, it has been recently shown through a connectomics study, that mushroom body extrinsic neurons and TU neurons have direct synaptic connections, suggesting that navigational information might get modulated by experience-dependent inputs in the CBU (Hulse et al., 2021; Li et al., 2020). In honeybees, mushroom body extrinsic neurons have also been shown to have ramifications into the superior neuropils (Rybak & Menzel, 1993). We therefore assume that a similar direct connection between the mushroom bodies and the CX also exists in honeybees. TU neurons were found in all layers of the CBU, except for layer IIb.

In the CBL, most identified neuronal cell types branched in layer I. This includes three types of tangential neuron (TL1, TL3 and TL6, ER or ring neurons in *Drosophila*) as well as two types of columnar neuron (CL2, CL1, in *Drosophila*: P-EN, E-PG). While the three tangential neuron types and the columnar CL2 neurons branch exclusively in layer CBL-I, CL1 neurons branch in the entire CBL. TL2 neurons, on the other hand, branch exclusively in layer II. In *Drosophila*, it has been shown, that P-EN neurons and E-PG neurons are part of the internal compass network that signals head direction with respect to an external frame of reference (Green et al., 2017; Seelig & Jayaraman, 2015; Turner-Evans et al., 2017). While E-PG (CL1) neurons signal current head direction through a single bump of activity within the ellipsoid body (CBL, Seelig & Jayaraman, 2015), P-EN (CL2) neurons are responsible for shifting this bump, when the animal turns. In addition to the head-direction signal, P-EN neurons signal rotation velocity (Green et al., 2017; Turner-Evans et al., 2017). We therefore suggest that rotation velocity signals of the compass network are processed in CBL-I in the honeybee, while the heading signal is processed in the entire CBL.

5 | CONCLUSION

Our study presents the first detailed three-dimensional atlas of the CX and associated neuropils of a bee. We demonstrate that a new method of constructing such an atlas yields a reliable volumetric representation of neuropils with volumes spanning roughly three orders of magnitude. Inclusion of peptidergic layers will facilitate the use of this atlas as a platform for neuroanatomical studies for other researchers.

ACKNOWLEDGMENTS

We are grateful to Dr. Uwe Homberg for helpful discussions about neuroanatomy, for reading an earlier version of the manuscript and for sharing antibodies that were kindly donated to him by Drs. Hans Agricola, Erich Buchner, Eve Marder, Julia Polak, and Christian Wegener.

We thank Drs. Wolfgang Rössler and Jens Habenstein for helpful discussions about neuroanatomy, Dr. Basil el Jundi for help with Amira, helpful discussions about neuroanatomy, and reading of the manuscript, Matheus Pagy for help with Osmium staining, and Jutta Seyfarth and Martina Kern for expert bee-keeping and technical assistance. Funding was obtained from the Deutsche Forschungsgemeinschaft (DFG), grant number: PF 714/4-1 and PF 714/5-1 to K. P. Further funding was obtained from FAPEMIG - Minas Gerais Research Funding Foundation, grant number APQ-02711-21 to T. M. Funding for the confocal laser scanning microscopes was obtained from the DFG, grant numbers: INST 93/829-1 FUGG (University of Würzburg, Leica TCS SP8) and INST 160/447-1 FUGG (University of Marburg, Leica TCS SP5).

Open access funding enabled and organized by Projekt DEAL.

CONFLICT OF INTEREST

The authors declare no conflict of interest.

AUTHOR CONTRIBUTION

K. P. designed and supervised the study. A. K., R. H., H. W., M. P., and T. M. acquired data. A. K., R. H., K. T., E. B., M. P., T. M., and K. P. analyzed and interpreted data. K. P. wrote the manuscript with contributions from R. H. and T. M. All authors reviewed the manuscript and approved its final version.

DATA AVAILABILITY STATEMENT

Data from this study are available at insectbraindb.org.

Standard atlas of central complex, including peptidergic layers of the central body (Figures 8 and 14): https://hdl.handle.net/20.500.12158/EIN-0000227.1

Confocal stack of antisynapsin-labeled central brain and corresponding 3D reconstruction (#1 in Figure 4): https://hdl.handle.net/20.500.12158/EIN-0000222.1

Confocal stack of anti-FMRFamide-labeled central brain and corresponding 3D reconstruction (Figure 9): https://hdl.handle.net/20.500.12158/EIN-0000235.1

Confocal stack of antiallatostatin-labeled central brain and corresponding 3D reconstruction (Figure 10): https://hdl.handle.net/20.500.12158/EIN-0000234.1

Confocal stack of antilocustatachykinin-labeled central brain and corresponding 3D reconstruction (Figure 12): https://hdl.handle.net/20.500.12158/EIN-0000237.1

Confocal stack of antigastrin/cholecystokinin-labeled central brain and corresponding 3D reconstruction (Figure 13): https://hdl.handle.net/20.500.12158/EIN-0000236.1

All other data are available from the corresponding author upon request.

REFERENCES

Adden, A., Wibrand, S., Pfeiffer, K., Warrant, E., & Heinze, S. (2020). The brain of a nocturnal migratory insect, the Australian bogong moth. *Journal of Comparative Neurology*, *528*(11), 1942–1963.

Beer, K., Kolbe, E., Kahana, N. B., Yayon, N., Weiss, R., Menegazzi, P., Bloch, G., & Helfrich-Förster, C. (2018). Pigment-dispersing factor-expressing neurons convey circadian information in the honey bee brain. *Open Biology*, *8*(1), 170224.

Beetz, M. J., el Jundi, B., Heinze, S., & Homberg, U. (2015). Topographic organization and possible function of the posterior optic tubercles in the brain of the desert locust *Schistocerca gregaria*. *Journal of Comparative Neurology*, *523*, 1589–1607.

Brandt, R., Rohlfing, T., Rybak, J., Krofczik, S., Maye, A., Westerhoff, M., Hege, H. - C., & Menzel, R. (2005). Three-dimensional average-shape atlas of the honeybee brain and its applications. *Journal of Comparative Neurology*, *492*, 1–19.

Davis, N. T., Homberg, U., Teal, P. E., Altstein, M., Agricola, H. - J., & Hildebrand, J. G. (1996). Neuroanatomy and immunocytochemistry of the median neuroendocrine cells of the subesophageal ganglion of the tobacco hawkmoth, *Manduca sexta*: Immunoreactivities to PBAN, and other neuropeptides. *Microscopy Research and Technique*, *35*, 201–229.

Dent, J. A., Polson, A. G., & Klymkowsky, M. W. (1989). A whole-mount immunocytochemical analysis of the expression of the intermediate filament protein vimentin in *Xenopus*. *Development (Cambridge, England)*, *105*, 61–74.

Dreyer, D., Vitt, H., Dippel, S., Goetz, B., el Jundi, B., Kollmann, M., Hütteroth, W., & Schachtner, J. (2010). 3D Standard Brain of the red flour beetle *Tribolium castaneum*: A tool to study metamorphic development and adult plasticity. *Frontiers in Systems Neuroscience*, *4*, 3.

Ehmer, B., & Gronenberg, W. (2002). Segregation of visual input to the mushroom bodies in the honeybee *(Apis mellifera)*. *Journal of Comparative Neurology*, *451*, 362–373.

el Jundi, B., & Heinze, S. (2020). Three-dimensional atlases of insect brains. In: Pelc, R., Walz, W., & Doucette, J. R., editors. *Neurohistology and Imaging Techniques*. New York, NY: Springer US. pp. 73–124.

el Jundi, B., Heinze, S., Lenschow, C., Kurylas, A., Rohlfing, T., & Homberg, U. (2010). The locust standard brain: A 3D standard of the central complex as a platform for neural network analysis. *Frontiers in Systems Neuroscience*, *3*, 21.

el Jundi, B., & Homberg, U. (2010). Evidence for the possible existence of a second polarization-vision pathway in the locust brain. *Journal of Insect Physiology*, *56*, 971–979.

el Jundi, B., Hütteroth, W., Kurylas, A. E., & Schachtner, J. (2009). Anisometric brain dimorphism revisited: Implementation of a volumetric 3D standard brain in *Manduca sexta*. *Journal of Comparative Neurology*, *517*, 210–225.

el Jundi, B., Warrant, E. J., Byrne, M. J., Khaldy, L., Baird, E., Smolka, J., & Dacke, M. (2015). Neural coding underlying the cue preference for celestial orientation. *PNAS*, *112*, 11395–11400.

el Jundi, B., Warrant, E. J., Pfeiffer, K., & Dacke, M. (2018). Neuroarchitecture of the dung beetle central complex. *Journal of Comparative Neurology*, *526*, 2612–2630.

Galizia, C. G., & Kreissl, S. (2012). Neuropeptides in honey bees. In: (Galizia, C. G., Eisenhardt, D., & Giurfa, M., Eds.), *Honeybee Neurobiology and Behavior*. Springer Netherlands: Dordrecht. pp. 211–226.

Green, J., Adachi, A., Shah, K. K., Hirokawa, J. D., Magani, P. S., & Maimon, G. (2017). A neural circuit architecture for angular integration in Drosophila. *Nature*, *546*, 101–106.

Groothuis, J., Pfeiffer, K., el Jundi, B., & Smid, H. M. (2019). The jewel wasp standard brain: Average shape atlas and morphology of the female *Nasonia vitripennis* brain. *Arthropod Structure and Development*, *51*, 41–51.

Hardcastle, B. J., Omoto, J. J., Kandimalla, P., Nguyen, B. - C. M., Keleş, M. F., Boyd, N. K., Hartenstein, V., & Frye, M. A. (2021). A visual pathway for skylight polarization processing in *Drosophila*. *eLife*, *10*, e63225.

Heinze, S., Florman, J., Asokaraj, S., el Jundi, B., & Reppert, S. M. (2013). Anatomical basis of sun compass navigation II: The neuronal composition of the central complex of the monarch butterfly. *Journal of Comparative Neurology*, *521*, 267–298.

Heinze, S., & Homberg, U. (2007). Maplike representation of celestial *E*-vector orientations in the brain of an insect. *Science*, *315*, 995–997.

Heinze, S., & Homberg, U. (2008). Neuroarchitecture of the central complex of the desert locust: Intrinsic and columnar neurons. *Journal of Comparative Neurology*, *511*, 454–478.

Heinze, S., & Reppert, S. M. (2011). Sun compass integration of skylight cues in migratory monarch butterflies. *Neuron*, *69*, 345–358.

Heinze, S., & Reppert, S. M. (2012). Anatomical basis of sun compass navigation I: The general layout of the monarch butterfly brain. *Journal of Comparative Neurology*, *520*, 1599–1628.

Held, M., Berz, A., Hensgen, R., Muenz, T. S., Scholl, C., Rössler, W., Homberg, U., & Pfeiffer, K. (2016). Microglomerular synaptic complexes in the sky-compass network of the honeybee connect parallel pathways from the anterior optic tubercle to the central complex. *Frontiers in Behavioural Neuroscience*, *10*, 186.

Held, M., Le, K., Pegel, U., Dersch, F., Beetz, M. J., Pfeiffer, K., & Homberg, U. (2020). Anatomical and ultrastructural analysis of the posterior optic tubercle in the locust *Schistocerca gregaria*. *Arthropod Structure & Development*, *58*, 100971.

Hensgen, R., England, L., Homberg, U., & Pfeiffer, K. (2020). Neuroarchitecture of the central complex in the brain of the honeybee: Neuronal cell types. *Journal of Comparative Neurology*, *105*, 61.

Homberg, U. (1985). Interneurones of the central complex in the bee brain (*Apis mellifera*, L.). *Journal of Insect Physiology*, *31*, 251–264.

Homberg, U., Davis, N. T., & Hildebrand, J. G. (1991). Peptide-immunocytochemistry of neurosecretory cells in the brain and retrocerebral complex of the sphinx moth *Manduca sexta*. *Journal of Comparative Neurology*, *303*, 35–52.

Homberg, U., Hofer, S., Pfeiffer, K., & Gebhardt, S. (2003). Organization and neural connections of the anterior optic tubercle in the brain of the locust, *Schistocerca gregaria*. *Journal of Comparative Neurology*, *462*, 415–430.

Homberg, U., & Würden, S. (1997). Movement-sensitive, polarization-sensitive, and light-sensitive neurons of the medulla and accessory medulla of the locust, *Schistocerca gregaria*. *Journal of Comparative Neurology*, *386*, 329–346.

Hu, W., Peng, Y., Sun, J., Zhang, F., Zhang, X., Wang, L., Li, Q., & Zhong, Y. (2018). Fan-shaped body neurons in the *Drosophila* brain regulate both innate and conditioned nociceptive avoidance. *Cell Reports*, *24*, 1573–1584.

Hulse, B. K., Haberkern, H., Franconville, R., Turner-Evans, D. B., Takemura, S. - Y., Wolff, T., Noorman, M., Dreher, M., Dan, C., Parekh, R., Hermundstad, A. M., Rubin, G. M., & Jayaraman, V. (2021). A connectome of the *Drosophila* central complex reveals network motifs suitable for flexible navigation and context-dependent action selection. *eLife*, *10*, e66039.

Ito, K., Shinomiya, K., Ito, M., Armstrong, J. D., Boyan, G., Hartenstein, V., Harzsch, S., Heisenberg, M., Homberg, U., Jenett, A., Keshishian, H., Restifo, L. L., Rössler, W., Simpson, J. H., Strausfeld, N. J., Strauss, R., &

Vosshall, L. B. (2014). A systematic nomenclature for the insect brain. *Neuron*, *81*, 755–765.

Jenett, A., Schindelin, J. E., & Heisenberg, M. (2006). The Virtual Insect Brain protocol: Creating and comparing standardized neuroanatomy. *Bmc Bioinformatics [Electronic Resource]*, *7*, 544.

Jonescu, C. N. (1909). Vergleichende Untersuchungen über das Gehirn der Honigbiene. *Jenaische Zeitschrift für Naturwissenschaft*, *45*, 111–180.

Kahsai, L., Martin, J. - R., & Winther, Å. M. E. (2010). Neuropeptides in the *Drosophila* central complex in modulation of locomotor behavior. *Journal of Experimental Biology*, *213*, 2256–2265.

Kahsai, L., & Winther, Å. M. E. (2011). Chemical neuroanatomy of the *Drosophila* central complex: Distribution of multiple neuropeptides in relation to neurotransmitters. *Journal of Comparative Neurology*, *519*, 290–315.

Kenyon, F. C. (1896). The brain of the bee. A preliminary contribution to the morphology of the nervous system of the Arthropoda. *Journal of Comparative Neurology*, *6*, 133–210.

Kinoshita, M., Pfeiffer, K., & Homberg, U. (2007). Spectral properties of identified polarized-light sensitive interneurons in the brain of the desert locust *Schistocerca gregaria*. *Journal of Experimental Biology*, *210*, 1350–1361.

Klagges, B. R., Heimbeck, G., Godenschwege, T. A., Hofbauer, A., Pflugfelder, G. O., Reifegerste, R., Reisch, D., Schaupp, M., Buchner, S., & Buchner, E. (1996). Invertebrate synapsins: A single gene codes for several isoforms in *Drosophila*. *Journal of Neuroscience*, *16*, 3154–3165.

Kreissl, S., & Bicker, G. (1989). Histochemistry of acetylcholinesterase and immunocytochemistry of an acetylcholine receptor-like antigen in the brain of the honeybee. *Journal of Comparative Neurology*, *286*, 71–84.

Kreissl, S., Strasser, C., & Galizia, C. G. (2010). Allatostatin immunoreactivity in the honeybee brain. *Journal of Comparative Neurology*, *518*, 1391–1417.

Kurylas, A. E., Rohlfing, T., Krofczik, S., Jenett, A., & Homberg, U. (2008). Standardized atlas of the brain of the desert locust, *Schistocerca gregaria*. *Cell and Tissue Research*, *333*, 125–145.

Li, F., Lindsey, J. W., Marin, E. C., Otto, N., Dreher, M., Dempsey, G., Stark, I., Bates, A. S., Pleijzier, M. W., Schlegel, P., Nern, A., Takemura, S. - Y., Eckstein, N., Yang, T., Francis, A., Braun, A., Parekh, R., Costa, M., Scheffer, L. K., …, & Rubin, G. M. (2020). The connectome of the adult *Drosophila* mushroom body provides insights into function. *eLife*, *9*, e62575.

Liu, G., Seiler, H., Wen, A., Zars, T., Ito, K., Wolf, R., Heisenberg, M., & Liu, L. (2006). Distinct memory traces for two visual features in the *Drosophila* brain. *Nature*, *439*, 551–556.

Lu, J., Behbahani, A. H., Hamburg, L., Westeinde, E. A., Dawson, P. M., Lyu, C., Maimon, G., Dickinson, M. H., Druckmann, S., & Wilson, R. I. (2022). Transforming representations of movement from body- to world-centric space. *Nature*, *601*, 98–104.

Lyu, C., Abbott, L. F., & Maimon, G. (2022). Building an allocentric travelling direction signal via vector computation. *Nature*, *601*, 92–97.

Marder, E., Calabrese, R. L., Nusbaum, M. P., & Trimmer, B. (1987). Distribution and partial characterization of FMRFamide-like peptides in the stomatogastric nervous systems of the rock crab, Cancer borealis, and the spiny lobster, *Panulirus interruptus*. *Journal of Comparative Neurology*, *259*, 150–163.

Milde, J. J. (1988). Visual responses of interneurones in the posterior median protocerebrum and the central complex of the honeybee *Apis mellifera*. *Journal of Insect Physiology*, *34*, 427–436.

Mobbs, P. G.. (1985). Brain structure. In: Kerkut, G. A., & Gilbert, L., editors. *Comprehensive insect physiology biochemistry and pharmacology*. pp. 299–370.

Mota, T., Yamagata, N., Giurfa, M., Gronenberg, W., & Sandoz, J. - C. (2011). Neural organization and visual processing in the anterior optic tubercle of the honeybee brain. *Journal of Neuroscience*, *31*, 11443–11456.

Nässel, D. R., & Homberg, U. (2006). Neuropeptides in interneurons of the insect brain. *Cell and Tissue Research*, *326*, 1–24.

Nässel, D. R., Kim, M. Y., & Lundquist, C. T. (1995). Several forms of callitachykinins are distributed in the central nervous system and intestine of the blowfly *Calliphora vomitoria*. *Journal of Experimental Biology*, *198*, 2527–2536.

Okubo, T., Patella, P., D'Alessandro, I., & Wilson, R. I. (2020). A neural network for wind-guided compass navigation. *Neuron*, *107*, 924–940. e18.

Ott, S. R. (2008). Confocal microscopy in large insect brains: Zinc-formaldehyde fixation improves synapsin immunostaining and preservation of morphology in whole-mounts. *Journal of Neuroscience Methods*, *172*, 220–230.

Pegel, U., Pfeiffer, K., & Homberg, U. (2018). Integration of celestial compass cues in the central complex of the locust brain. *Journal of Experimental Biology*, *221*, jeb171207.

Pegel, U., Pfeiffer, K., Zittrell, F., Scholtyssek, C., & Homberg, U. (2019). Two compasses in the central complex of the locust brain. *Journal of Neuroscience*, *39*, 3070–3080.

Petri, B., Stengl, M., Würden, S., & Homberg, U. (1995). Immunocytochemical characterization of the accessory medulla in the cockroach *Leucophaea maderae*. *Cell and Tissue Research*, *282*, 3–19.

Pfeiffer, K., & Homberg, U. (2007). Coding of azimuthal directions via time-compensated combination of celestial compass cues. *Current Biology*, *17*, 960–965.

Pfeiffer, K., & Homberg, U. (2014). Organization and functional roles of the central complex in the insect b rain. *Annual Review of Entomology*, *59*, 165–184.

Pfeiffer, K., & Kinoshita, M. (2012). Segregation of visual inputs from different regions of the compound eye in two parallel pathways through the anterior optic tubercle of the bumblebee *(Bombus ignitus)*. *Journal of Comparative Neurology*, *520*, 212–229.

Pfeiffer, K., Kinoshita, M., & Homberg, U. (2005). Polarization-sensitive and light-sensitive neurons in two parallel pathways passing through the anterior optic tubercle in the locust brain. *Journal of Neurophysiology*, *94*, 3903–3915.

Rein, K., Zöckler, M., Mader, M. T., Grübel, C., & Heisenberg, M. (2002). The *Drosophila* Standard Brain. *Current Biology*, *12*, 227–231.

Rohlfing, T., Brandt, R., Maurer, C. R., & Menzel, R.. (2001). Bee brains, B-splines and computational democracy: generating an average shape atlas. Proceedings of the IEEE Workshop on Mathematical Methods in Biomedical Image Analysis, MMBIA, Kauai, Hawaii, December, 2001, 187–194.

Rohlfing, T., & Maurer, C. R. (2003). Nonrigid image registration in shared-memory multiprocessor environments with application to brains, breasts, and bees. *IEEE Transactions on Information Technology in Biomedicine*, *7*, 16–25.

Rohlfing, T., & Maurer, C. R. (2007). Shape-based averaging. *IEEE Transactions on Image Process*, *16*, 153–161.

Rother, L., Kraft, N., Smith, D. B., el Jundi, B., Gill, R. J., & Pfeiffer, K. (2021). A micro-CT-based standard brain atlas of the bumblebee. *Cell and Tissue Research*, *386*, 29–45.

Rybak, J., & Menzel, R. (1993). Anatomy of the mushroom bodies in the honey bee brain: The neuronal connections of the alpha-lobe. *Journal of Comparative Neurology*, *334*, 444–465.

Sakura, M., Lambrinos, D., & Labhart, T. (2008). Polarized skylight navigation in insects: Model and electrophysiology of e-vector coding by neurons in the central complex. *Journal of Neurophysiology*, *99*, 667–682.

Sareen, P. F., McCurdy, L. Y., & Nitabach, M. N. (2021). A neuronal ensemble encoding adaptive choice during sensory conflict in *Drosophila*. *Nature Communications*, *12*, 4131.

Sayre, M. E., Templin, R., Chavez, J., Kempenaers, J., & Heinze, S. (2021). A projectome of the bumblebee central complex. *eLife*, *10*, e68911.

Schäfer, S., & Rehder, V. (1989). Dopamine-like immunoreactivity in the brain and suboesophageal ganglion of the honeybee. *Journal of Comparative Neurology*, *280*, 43–58.

Schürmann, F. W., & Erber, J. (1990). FMRFamide-like immunoreactivity in the brain of the honeybee *(Apis mellifera)*. A light-and electron microscopical study. *Neuroscience*, *38*, 797–807.

Seelig, J. D., & Jayaraman, V. (2015). Neural dynamics for landmark orientation and angular path integration. *Nature*, *521*, 186–191.

Siju, K. P., Reifenrath, A., Scheiblich, H., Neupert, S., Predel, R., Hansson, B. S., Schachtner, J., & Ignell, R. (2014). Neuropeptides in the antennal lobe of the yellow fever mosquito, *Aedes aegypti*. *Journal of Comparative Neurology*, *522*, 592–608.

Stengl, M., & Homberg, U. (1994). Pigment-dispersing hormone-immunoreactive neurons in the cockroach *Leucophaea maderae* share properties with circadian pacemaker neurons. *Journal of Comparative Physiology A*, *175*, 203–213.

Stone, T., Webb, B., Adden, A., Weddig, N. B., Honkanen, A., Templin, R., Wcislo, W., Scimeca, L., Warrant, E., & Heinze, S. (2017). An anatomically constrained model for path integration in the bee brain. *Current Biology*, *27*, 3069–3085.e11.

Strausfeld, N. J., Homberg, U., & Kloppenburg, P. (2000). Parallel organization in honey bee mushroom bodies by peptidergic kenyon cells. *Journal of Comparative Neurology*, *424*, 179–195.

Tang, Q. - B., Song, W. - W., Chang, Y. - J., Xie, G. - Y., Chen, W. - B., & Zhao, X. - C. (2019). Distribution of serotonin-immunoreactive neurons in the brain and gnathal ganglion of caterpillar *Helicoverpa armigera*. *Frontiers in Neuroanatomy*, *13*, 56.

Timm, J., Scherner, M., Matschke, J., Kern, M., & Homberg, U. (2021). Tyrosine hydroxylase immunostaining in the central complex of dicondylian insects. *Journal of Comparative Neurology*, *529*, 3131–3154.

Turner-Evans, D., Wegener, S., Rouault, H., Franconville, R., Wolff, T., Seelig, J. D., Druckmann, S., & Jayaraman, V. (2017). Angular velocity integration in a fly heading circuit. *eLife*, *6*, e23496.

Veenstra, J. A., Lau, G. W., Agricola, H. J., & Petzel, D. H. (1995). Immunohistological localization of regulatory peptides in the midgut of the female mosquito *Aedes aegypti*. *Histochemistry and Cell Biology*, *104*, 337–347.

Vitzthum, H., & Homberg, U. (1998). Immunocytochemical demonstration of locustatachykinin-related peptides in the central complex of the locust brain. *Journal of Comparative Neurology*, *390*, 455–469.

Vitzthum, H., Homberg, U., & Agricola, H. (1996). Distribution of Dip-allatostatin I-like immunoreactivity in the brain of the locust *Schistocerca gregaria* with detailed analysis of immunostaining in the central complex. *Journal of Comparative Neurology*, *369*, 419–437.

von Frisch, K. (1965). *Tanzsprache und Orientierung der Bienen*. Springer.

Vries, L. D., K, P., Trebels, B., Adden, A. K., Green, K., Warrant, E., & Heinze, S. (2017). Comparison of navigation-related brain regions in migratory versus non-migratory noctuid moths. *Frontiers in Behavioural Neuroscience*, *11*, 158.

Wei, H., el Jundi, B., Homberg, U., & Stengl, M. (2010). Implementation of pigment-dispersing factor-immunoreactive neurons in a standardized atlas of the brain of the cockroach *Leucophaea maderae*. *Journal of Comparative Neurology*, *518*, 4113–4133.

Weir, P. T., & Dickinson, M. H. (2015). Functional divisions for visual processing in the central brain of flying *Drosophila*. *PNAS*, *112*, E5523–E5532.

Wolff, T., Iyer, N. A., & Rubin, G. M. (2015). Neuroarchitecture and neuroanatomy of the Drosophila central complex: A GAL4-based dissection of protocerebral bridge neurons and circuits. *Journal of Comparative Neurology*, *523*, 997–1037.

Würden, S., & Homberg, U. (1995). Immunocytochemical mapping of serotonin and neuropeptides in the accessory medulla of the locust, *Schistocerca gregaria*. *Journal of Comparative Neurology*, *362*, 305–319.

Xie, X., Tabuchi, M., Corver, A., Duan, G., Wu, M. N., & Kolodkin, A. L. (2019). Semaphorin 2b regulates sleep-circuit formation in the *Drosophila* central brain. *Neuron*, *104*, 322–337.e14.

Zeller, M., Held, M., Bender, J., Berz, A., Heinloth, T., Hellfritz, T., & Pfeiffer, K. (2015). Transmedulla neurons in the sky compass network of the honeybee *(Apis mellifera)* are a possible site of circadian input. *PloS One*, *10*, e0143244.

How to cite this article: Kaiser, A., Hensgen, R., Tschirner, K., Beetz, E., Wüstenberg, H., Pfaff, M., Mota, T., & Pfeiffer, K. (2022). A three-dimensional atlas of the honeybee central complex, associated neuropils and peptidergic layers of the central body. *Journal of Comparative Neurology*, *530*, 2416–2438. https://doi.org/10.1002/cne.25339